sustainability

MDPI

Article

Mechanical Performance, Thermal Resistance, and Durability of Red Mud-Based Cement Mortar Incorporating Fly Ash, Basalt Fibers, and Nano Zinc Oxide

Sultan Almuaythir [1], Mousa Shhabat [2,3], Ahmed Ashteyat [1,*] and Abdelmalek H. Aljarah [4]

[1] Department of Civil Engineering, College of Engineering in Al-Kharj, Prince Sattam Bin Abdulaziz University, Al-Kharj 11942, Saudi Arabia; s.alhomair@psau.edu.sa
[2] Department of Civil Engineering, Faculty of Engineering, The University of Jordan, Amman 11942, Jordan; mos8200833@ju.edu.jo
[3] Greater Irbid Municipality, Irbid 21110, Jordan
[4] Department of Civil, Architectural and Environmental Engineering, Illinois Institute of Technology, Chicago, IL 60616, USA; aaljarah@hawk.illinoistech.edu
* Correspondence: a.ashteyat@psau.edu.sa

Abstract

Red mud (RM), a highly alkaline by-product of the alumina refining process, poses significant environmental challenges due to its large-scale accumulation. This study systematically investigates the mechanical performance, thermal resistance, and durability of RM-based cement mortar, evaluating the individual effects of fly ash (FA), basalt fibers (BF), and nano zinc oxide (NZO) as separate modifying constituents introduced independently into the RM matrix. Fourteen mortar mixtures were prepared with RM replacement levels of 10–35%, a constant FA content of 15%, BF dosages of 0.5–1.5%, and NZO dosages of 0.5–2.0%. Workability, 28-day compressive and flexural strengths, residual mechanical properties after exposure to 600 °C and 800 °C, sulfate resistance, and microstructural characteristics were evaluated. Increasing RM content reduced workability and mechanical strength, with compressive and flexural reductions reaching 35.5% and 29.0% at 30% RM, respectively. FA partially compensated through its ball-bearing effect and pozzolanic reactivity. The optimal 1.5% BF dosage increased the compressive and flexural strengths by 14.7% and 37.5%, respectively, and significantly enhanced the residual performance at elevated temperatures. The optimal 0.5% NZO improved the compressive and flexural strengths by 13.2% and 18.3%, respectively; however, 2.0% NZO caused complete strength loss, which may be associated with severe nanoparticle agglomeration and possible zinc-containing reaction products reported in previous studies. The formation of specific crystalline phases was not experimentally verified in the present study. Sulfate resistance deteriorated with increasing RM, whereas 1.5% BF and 1.0% NZO reduced mass loss by 58.9% and 59.7%, respectively. SEM confirmed that RM15 + FA15 exhibited the densest microstructure with minimal voids. The results demonstrate that RM can be effectively utilized as a sustainable cement replacement, with FA, BF, and NZO each independently identified as effective performance-enhancing constituents at their respective optimal dosages; their combined quaternary application remains untested and is proposed as a direction for future validation.

Keywords: red mud; fly ash; basalt fiber; nanomaterial; cement mortar; mechanical performance; thermal resistance; sulfate resistance; microstructure; sustainable construction

Check for updates

Academic Editor: Meenesh R. Singh

Received: 21 June 2026
Revised: 8 August 2026
Accepted: 17 August 2026
Published: 20 August 2026

Copyright: © 2026 by the authors. Licensee MDPI, Basel, Switzerland. This article is an open access article distributed under the terms and conditions of the Creative Commons Attribution (CC BY) license.

1. Introduction

The construction and building materials industry is under increasing pressure to reduce its environmental footprint while simultaneously improving material performance and longevity. Ordinary Portland Cement (OPC) production accounts for approximately 8% of global CO_2 emissions, generating nearly 0.9 tons of CO_2 per ton of clinker produced [1–3]. This reality has accelerated the search for supplementary cementitious materials (SCMs), which are industrial by-products that can partially replace cement while preserving or enhancing mechanical and durability performance. Among the most promising candidates are red mud (RM), fly ash (FA), basalt fibers (BF), and nano-scale oxides such as nano zinc oxide (NZO), each of which contributes distinct physicochemical benefits to cementitious matrices.

Red mud (RM), also known as bauxite residue, is a highly alkaline by-product generated during the Bayer process for alumina extraction from bauxite ore. Owing to its substantial production volume and caustic nature (pH ≈ 12–13), RM represents a major environmental challenge worldwide. Approximately 1–1.5 tons of RM are produced per ton of alumina, with nearly 150 million tons generated from 115 million tons of alumina in 2015 alone [4,5]. By 2023, the cumulative global stockpile exceeded 5 billion tons and continues to increase at an annual rate of approximately 180 million tons, whereas the utilization rate remains below 15% [6]. These numbers highlight the critical concerns related to long-term storage, land occupation, and potential environmental contamination. The chemical composition of RM varies depending on the bauxite source and refining conditions; however, it typically consists of 20–30% iron oxides (Fe_2O_3), 20–30% alumina (Al_2O_3), 10–20% silica (SiO_2), and minor constituents such as titanium dioxide (TiO_2) and calcium oxide (CaO) [7]. Its fine particle size, high alkalinity, and mineralogical composition have stimulated extensive research into its valorization for cementitious applications.

In cementitious systems, RM has been investigated as a supplementary cementitious material (SCM). Low replacement levels (≤10%) generally maintain mechanical performance without significant strength loss [8], and enhanced durability in aggressive environments has been reported [9]. Blending RM with other industrial by-products, such as fly ash (FA), has further improved the performance of composite binders [10]. To enhance reactivity, thermal activation and alkali-activated systems have been widely explored. Studies have examined RM as a component in Portland cement blends [11,12] and calcined cement systems [13,14]. Thermal treatment at elevated temperatures modifies mineral phases and increases amorphous content; 800 °C has been identified as an optimal calcination temperature, with 10% addition yielding favorable mechanical performance. In alkali-activated slag (AAS) mortars, 20% RM replacement provided optimal compressive strength development, although flexural strength decreased at higher RM contents [15]. Calcined RM also improved strength development and significantly reduced autogenous and drying shrinkage in alkali-activated fly ash slag (AAFS) systems [16]. However, long-term performance may be adversely affected at higher replacement ratios, with increased porosity, water absorption, and reduced compressive strength reported over extended curing periods [17]. Overall, these studies confirm that RM possesses significant potential as a sustainable SCM when appropriately treated and optimized; nevertheless, challenges related to high alkalinity, compositional variability, workability reduction at higher dosages, and long-term durability remain critical considerations.

Fly ash (FA), a by-product of coal-fired power generation, is one of the most extensively studied SCMs in cementitious systems. Its spherical particle morphology improves fresh-state workability and reduces water demand, while its amorphous silica- and alumina-rich chemistry promotes secondary pozzolanic reactions with calcium hydroxide ($Ca(OH)_2$) liberated during cement hydration, yielding additional calcium silicate hydrate (C–S–H) and refining pore structure [18]. Class F fly ash, characterized by SiO_2 + Al_2O_3 + Fe_2O_3 content exceeding 70%, has demonstrated consistent strength development and durability

improvements in mortar and concrete when used at replacement levels of 15–30% [19]. Studies incorporating FA alongside RM have reported synergistic benefits: the alkalinity of RM can serve as an internal activator for FA's latent pozzolanic reactivity, which may be associated with the formation of C–A–S–H and N–A–S–H gels by analogy with previous RM–FA studies [20,21]; however, no XRD, FTIR, or SEM-EDS analysis was performed in this study to confirm their presence [20,21]. Moreover, FA incorporation in RM-blended systems has been shown to mitigate the adverse effects of RM's high iron oxide content on early-age strength development [22]. Despite its well-established benefits, FA at high replacement ratios tends to retard early-age strength development due to its slow pozzolanic reaction kinetics, necessitating careful mix optimization [23].

The incorporation of short discontinuous fibers into cementitious matrices is a well-established strategy to overcome their inherent brittleness and limited tensile capacity. Among the available fiber types, basalt fibers (BF), derived from the melt of volcanic basalt rock at temperatures around 1400–1500 °C, have attracted significant research attention owing to their outstanding mechanical and chemical properties [24]. Basalt fibers exhibit tensile strengths in the range of 2500–4800 MPa, an elastic modulus of 65–110 GPa, and superior chemical resistance in alkaline cementitious environments compared with glass or polymer fibers [25,26]. Their natural volcanic origin and relatively simple manufacturing process confer a more favorable ecological profile, with significantly lower embodied energy than carbon or aramid fibers [27]. In cement mortar and concrete systems, BF addition at dosages of 0.5–2.0% by volume has consistently been shown to improve compressive and flexural strengths, fracture toughness, and post-crack ductility through crack-bridging and stress-transfer mechanisms [28,29]. The fiber–matrix interfacial bonding in BF-reinforced composites is governed by mechanical interlocking and chemical interaction with cement hydration products, which can be further enhanced through surface treatment or sizing [30]. Importantly, basalt fibers exhibit remarkable thermal stability up to 700–800 °C, retaining significant tensile capacity at elevated temperatures and thereby enhancing the residual mechanical performance and fire resistance of reinforced mortar systems [31,32]. Studies on BF-reinforced mortars and concretes subjected to elevated temperatures consistently demonstrate superior residual compressive and flexural strengths compared with plain or polymer-fiber-reinforced counterparts [33,34]. At the nanoscale, the incorporation of nano-sized particles represents a frontier strategy for tailoring the microstructure of cementitious composites. Nano zinc oxide (NZO) is a multifunctional inorganic nanoparticle with a particle size typically in the range of 20–100 nm and a high specific surface area, enabling it to act simultaneously as a nano-filler, nucleation accelerator, and pozzolanic agent within the cement matrix [35,36]. The nano-filling effect of NZO densifies the interfacial transition zone (ITZ) and capillary pore network, reducing permeability and enhancing resistance to aggressive ion ingress [37]. The nucleation effect accelerates cement hydration by providing additional surface area for C–S–H precipitation, resulting in strength gains at both early and late curing ages [38]. Studies have reported compressive strength improvements of 10–20% in NZO-modified mortar and concrete at optimal dosages, typically in the range of 0.5–2.0% by weight of total binder, with diminishing returns or strength reductions at higher dosages due to nanoparticle agglomeration [39,40]. However, the behavior of NZO in systems containing high proportions of RM, which itself introduces reactive iron and alumina phases, remains incompletely understood, particularly its effect on high-temperature performance and the potential for explosive spalling from vapor pressure build-up within a densified matrix [41].

The individual and synergistic mechanisms of RM, FA, BF, and NZO are inferred to collectively govern the performance of the investigated cement mortar system, based on the measured mechanical and durability trends rather than direct mineralogical evidence. RM is

expected to provide a highly alkaline environment capable of activating the latent pozzolanic reactivity of FA, while its Fe- and Al-rich phases may contribute reactive compounds and, at higher replacement levels, a micro-filler effect; however, excess RM content promotes a more porous and heterogeneous microstructure, consistent with the SEM observations. FA, owing to its smooth spherical particle morphology, reduces inter-particle friction and water demand through a ball-bearing effect that improves fresh-state flow, while its pozzolanic reaction with calcium hydroxide is understood to generate secondary C–S–H, a reaction believed to depend on the alkaline activation supplied by RM. BF forms a random three-dimensional fiber network that is expected to bridge and arrest microcracks, thereby restraining crack propagation, limiting sulfate-ion ingress pathways, and enhancing residual strength and spalling resistance under elevated-temperature exposure, consistent with the measured mechanical and durability trends. NZO is understood to contribute both a nano-filler effect, blocking capillary pores and refining the interfacial transition zone, and a nucleation effect that may accelerate C–S–H precipitation, densifying the matrix around the BF network at optimum dosage. The interaction of these four mechanisms is proposed to collectively govern the workability, mechanical strength, thermal resistance, and sulfate durability of the resulting cement mortar system; it should be noted, however, that these mechanistic interpretations remain inferential, as no XRD, FTIR, TG/DSC, or SEM-EDS analysis was performed to directly verify the underlying reaction products or phase transformations, and this framework should therefore be regarded as a hypothesis for future validation (see Section 6). The water-to-binder ratio further governs both fresh- and hardened-state behavior: a higher ratio reduces yield stress and viscosity, improving flow and filling capacity, whereas hydrated microstructure development remains highly sensitive to the rheological regime established at mixing, as similarly demonstrated for cementitious grout propagation in fractured media [23]. Such rheological sensitivity to water content and mix consistency parallels the mechanisms controlling nanoparticle-induced pore refinement, whereby densification of the flow path and reduction of the effective permeable network are jointly governed by fluid rheology and particle-scale filling behavior.

Despite extensive research on red mud (RM), fly ash (FA), basalt fibers (BF), and nano zinc oxide (NZO) individually, no previous study has systematically screened the individual effects of FA, BF, and NZO within a single RM-based cement mortar framework under mechanical, thermal, and durability conditions. The novelty of the present study lies in this systematic single-variable evaluation, which isolates the individual contribution of each constituent to fresh-state behavior, mechanical performance, elevated-temperature resistance, and sulfate durability**, establishing an evidence-based foundation for future multi-component optimization**. The incorporation of RM, FA, BF, and NZO reflects distinct, independently evaluated mechanisms—alkaline activation of FA by RM within the RM–FA series, and crack-bridging (BF) or matrix-densification (NZO) effects introduced separately into the RM30 baseline; the potential interaction among BF, NZO, and FA within a single quaternary matrix remains untested and is identified as a key direction for future work. In particular, the influence of NZO-induced densification on high-temperature spalling behavior in RM-based systems has not previously been reported. Accordingly, this study investigates the fresh-state workability, compressive and flexural strengths, residual mechanical performance after elevated-temperature exposure, sulfate resistance, and microstructural characteristics of RM-based cement mortars incorporating FA, BF, and NZO at systematically varied proportions. Fourteen mortar mixtures were prepared with RM replacement levels of 10–35%, a constant 15% FA content, basalt fiber dosages of 0.5–1.5%, and NZO contents of 0.5–2.0%. The findings aim to support the development of sustainable and high-performance cementitious composites through the valorization of industrial waste materials and reduced reliance on conventional Portland cement.

2. Materials

2.1. Cement

Ordinary Portland Cement (OPC) Type I (Lafarge Holcim, Amman, Jordan) was used as the primary binding material in all mortar mixtures. The cement was sourced from a local Saudi manufacturer and complies with the requirements of ASTM C150 [42]. The chemical composition of the cement, as provided by the manufacturer, is presented in Table 1.

Table 1. Chemical composition of Ordinary Portland Cement (OPC) Type I.

Chemical Component	CaO	SiO_2	Al_2O_3	Fe_2O_3	SO_3	MgO	Na_2O	LOI
Percentage (%)	63.25	20.49	5.52	3.42	2.14	1.75	0.26	2.53

2.2. Red Mud

Red mud (RM) is a strongly alkaline industrial by-product (pH ≈ 12–13) generated during the Bayer process for alumina extraction from bauxite ore. The RM used in this study was supplied by (Ma'aden Aluminum Company, Ras Al Khair Industrial City, Saudi Arabia). Prior to use, the RM was air-dried under laboratory conditions to remove excess moisture, as shown in Figure 1. The dried material was subsequently ground, pulverized, and sieved through a No. 40 sieve (425 µm opening) to achieve a uniform particle size distribution suitable for mortar preparation. The chemical composition of RM, determined by X-ray fluorescence (XRF) analysis and expressed as a percentage of dry mass, is presented in Table 2. The results indicate that Al_2O_3, Fe_2O_3, and SiO_2 are the dominant constituents, collectively accounting for approximately 68% of the total composition, reflecting the alumino-silicate ferruginous nature of the material. Minor oxides including Na_2O, TiO_2, and CaO were each present at levels not exceeding 11%. The high alkalinity of RM, attributed primarily to its elevated Na_2O content (~10.83%), is a key characteristic that influences its interaction with cement hydration products and its potential role as an internal activator for supplementary cementitious materials in the composite mortar system.



Figure 1. Red mud.

Table 2. Chemical composition of red mud.

Elements	Percentage (%)
CaO	4.9
Fe_2O_3	23.79
SiO_2	17.9
Al_2O_3	26.24
Na_2O	10.83
TiO_2	7.50
LOI	5.96

2.3. Fly Ash

Class F fly ash (FA), a coal combustion by-product, was used as a supplementary cementitious material (SCM) at a constant replacement level of 15% by weight of total binder.

The FA was obtained from Builmix Company, Al Khobar, Saudi Arabia. Its incorporation was intended to improve particle packing, enhance pozzolanic reactivity, and mitigate early-age strength reduction associated with high RM contents. The physical properties and chemical composition of the FA, determined in accordance with ASTM C618 [43], are presented in Tables 3 and 4, respectively.

Table 3. Physical Properties of Class F Fly Ash.

Properties	Value
Appearance	Gray or Shaded Brown
Specific Surface (m^2/Kg)	345–380
Specific Gravity	2.35
Chloride content (%)	0.01
Flammability	Non-Flammable

Table 4. Chemical composition of Fly Ash.

Parameters	Method	Results	Requirement ASTM C618 Limits		
			Class N	Class F	Class C
Loss On Ignition	ASTM C311 [44]	2.12	10.0 max	6.0 max	6.0 max
Moisture content		0.32	3.0 max	3.0 max	3.0 max
Calcium oxide, CaO	Wavelength-dispersive X-ray fluorescence (ASTM E1621) [45]	4.02	-	18.0 max	>18.0
Silicon Oxide, SiO_2		52.59	-	-	-
Aluminum Oxide, Al_2O_3		30.81	-	-	-
Iron Oxide, Fe_2O_3 (%)		6.15	-	-	-
Sum (SiO_2 + Al_2O_3 + Fe_2O_3) (%)		90	70 min	70 min	50 min
Magnesium Oxide, MgO (%)		1.85	-	-	-
Sulfur Trioxide, SO_3 (%)		0.82	4.0 max	5.0 max	5.0 max
Chlorine, Cl (%)		0.03	-	-	-
Phosphorus pentoxide, P_2O_5 (%)		0.15	-	-	-
Manganese oxide, MnO (%)		0.17	-	-	-
Sodium Oxide, Na_2O (%)		0.33	-	-	-
Potassium Oxide K_2O (%)		0.59	-	-	-
Sodium oxide Equivalent (Na_2O + 0.658×K_2O) (%)		0.72	-	-	-

2.4. Basalt Fibers

Chopped basalt fibers (BF) were used as discontinuous reinforcing elements in selected mortar mixtures. The fibers were supplied by Globmarble Co. (Brooklyn, NY, USA) with a nominal length of 12 mm. They were selected for their high tensile strength (2600 MPa), high elastic modulus (≥65 GPa), excellent thermal stability (melting point 1450 °C), and superior chemical resistance in alkaline environments, making them well-suited for RM-based mortar systems. The fibers are shown in Figure 2, and their physical and mechanical properties are summarized in Table 5.

Table 5. Physical properties of basalt fiber.

Property	Value
Shape of Fiber	Straight
Density	2.67 (g/cm^3)
Length	12 mm
Diameter	16 microns
Melting Temperature	1450 °C
Tensile Strength	2600 MPa
Young's Modulus	≥65 GPa



Figure 2. Basalt fiber.

2.5. Nano Zinc Oxide

Nano zinc oxide (NZO) powder was used as a nanoparticle modifier to enhance the microstructural and mechanical properties of the RM-based mortar. The NZO was incorporated at dosage levels of 0.5%, 1.0%, and 2.0% by weight of total binder. The physical properties of NZO, as confirmed by the manufacturer's specifications, are presented in Table 6. The ultrafine particle size of NZO enables it to act as a nano-filler and nucleation accelerator. Previous studies have reported that NZO may promote C–S–H precipitation at appropriate dosages and improve mechanical performance at optimized dosage levels. The NZO powder used in this study is shown in Figure 3.

Table 6. Physical properties of nano zinc oxide (NZO).

Property	Value
Particle size (nm)	30–80
Purity (%)	≥99
Appearance	White powder



Figure 3. Nano Zinc Oxide.

3. Experimental Work

The experimental program was designed to assess the fresh-state workability, mechanical performance, high-temperature behavior, microstructural characteristics, and durability of red mud (RM)-based cement mortar incorporating FA, BF, and NZO. A total of fourteen mortar mixtures were developed with varying proportions of these constituents. The compressive and flexural strengths were evaluated after 28 days of standard water curing, as well as after exposure to elevated temperatures of 600 °C and 800 °C, to assess residual mechanical performance and fire resistance. Additional tests included flow, sulfate resistance, and scanning electron microscopy (SEM) analysis. All tests were conducted in accordance with the relevant ASTM standards, as detailed in the following subsections.

3.1. Mix Proportioning

A total of fourteen mortar mixtures were developed in this study. Red mud was used as a partial replacement for cement at levels of 10–35% by weight of total binder, while

fly ash was maintained at a constant replacement level of 15% in selected mixtures. Basalt fibers were incorporated at three dosage levels of 0.5%, 1.0%, and 1.5% by weight of total binder, and nano zinc oxide was added at contents of 0.5%, 1.0%, and 2.0% by weight of total binder. The NZO dosage range was selected based on ranges commonly reported in published literature on nanoparticle-modified cementitious systems [35,39,40]; the 2.0% dosage was included to explore the upper boundary of NZO application within this specific RM-based matrix, and the complete mechanical failure observed at this dosage is reported as a boundary-condition finding that defines the upper safe limit of NZO incorporation in RM-based mortars. The water-to-binder (w/b) ratio was kept constant at 0.48 for all mixtures. The mix proportions of all investigated mixtures are presented in Table 7. Prior to mixing, RM was air-dried under laboratory conditions, ground, and sieved through a No. 40 sieve (425 µm) to achieve a uniform particle size. RM and FA were dry-mixed thoroughly before the addition of other constituents. The mixing sequence adopted was as follows: cement and RM were first introduced into the mixer with half the water portion and mixed for 2 min; fine aggregate was then added with the remaining water, and mixing continued for a further 2 min until a homogeneous mixture was obtained. Basalt fibers and nano zinc oxide were added at the appropriate stage based on the mix design.

Table 7. Mix proportions of mortar mixtures.

Mixture	Water (Kg)	Cement (Kg)	Fine Aggregate (Kg)	Fly Ash (Kg)	Red Mud (Kg)	Basalt Fiber (Kg)	NZO (Kg)
C	1.2	2.5	6.875	0	0	0	0
RM0 + FA15	1.2	2.125	6.875	0.375	0	0	0
RM10 + FA15	1.2	1.875	6.875	0.375	0.25	0	0
RM15 + FA15	1.2	1.75	6.875	0.375	0.375	0	0
RM20 + FA15	1.2	1.625	6.875	0.375	0.5	0	0
RM25	1.2	1.875	6.875	0	0.625	0	0
RM30	1.2	1.75	6.875	0	0.75	0	0
RM35	1.2	1.625	6.875	0	0.875	0	0
RM30 + 0.5BF	1.2	1.75	6.875	0	0.75	0.0125	0
RM30 + 1BF	1.2	1.75	6.875	0	0.75	0.025	0
RM30 + 1.5BF	1.2	1.75	6.875	0	0.75	0.0375	0
RM30 + 0.5NZO	1.2	1.75	6.875	0	0.75	0	0.0125
RM30 + 1NZO	1.2	1.75	6.875	0	0.75	0	0.025
RM30 + 2NZO	1.2	1.75	6.875	0	0.75	0	0.05

3.2. Specimen Preparation and Curing

After mixing, the fresh mortar was cast into steel molds of two sizes—50 × 50 × 50 mm cubic molds for compressive strength and sulfate resistance tests and 100 × 100 × 400 mm prismatic molds for flexural strength testing—as shown in Figure 4. Three replicate specimens were prepared for each mixture to ensure statistical reliability of the results. All specimens were consolidated by vibration on a standard vibrating table, and the surfaces were finished using a trowel. The molds were kept at room temperature for 24 h, after which they were demolded and transferred to a water curing tank at 23 ± 2 °C for 28 days prior to testing.



Figure 4. Steel molds filled with red mud-based mortar.

3.3. Testing Methods

3.3.1. Flow Test

The fresh-state workability of the mortar mixtures was assessed using the flow test, conducted in accordance with ASTM C1437 [46]. A standard flow table was used for this purpose. The mortar was placed into a standard conical mold in two equal layers, with each layer compacted using 20 uniform tamps. The molds were then carefully lifted, and the flow table dropped 25 times within 15 s. The resulting spread diameter of the mortar was measured in two perpendicular directions, and the average value was recorded. The flow value was calculated as a percentage using the following Equation (1):

$$\text{Flow}(\%) = \frac{\text{D} - \text{Do}}{\text{Do}} \times 100 \quad (1)$$

where D is the average spread diameter after dropping (mm) and D_o is the base diameter of the conical mold (70 mm).

3.3.2. Mechanical Properties

The compressive and flexural strengths of the mortar specimens were evaluated after 28 days of water curing. Compressive strength was determined on 50 × 50 × 50 mm cubic specimens in accordance with ASTM C109/C109M [47], using a calibrated UTEST compression testing machine at a loading rate of 900 N/s, as illustrated in Figure 5. Flexural strength was assessed on 100 × 100 × 400 mm prismatic specimens in accordance with ASTM C348 [48], under a three-point loading configuration at a loading rate of 2.4 kN/min. The reported values represent the average of three replicate specimens for each mixture.



Figure 5. Compression testing machine.

3.3.3. Elevated Temperature Exposure

The residual mechanical performance of the mortar mixtures was evaluated after exposure to elevated temperatures of 600 °C and 800 °C. After 28 days of water curing, the specimens were placed in an electric furnace and heated from room temperature at a rate of 5 °C/min to each target temperature. Upon reaching the target temperature, the specimens were held isothermally for one hour to ensure uniform heat distribution throughout the specimen cross-section in accordance with the International Organization for Standardization (ISO-834) [49]. Following thermal exposure, the specimens were removed from the furnace and allowed to cool naturally to room temperature in ambient air before testing. The residual compressive and flexural strengths were then determined using the same procedures described in Section 3.3.2. The electric furnace used in this study is shown in Figure 6.



Figure 6. Oven.

3.3.4. Sulfate Resistance Test

The sulfate resistance of the mortar specimens was evaluated after 28 days of water curing; the initial dry mass of each specimen (W_0) was recorded prior to immersion. The specimens were then fully immersed in a 5% sodium sulfate (Na_2SO_4) solution for 28 days at room temperature. At the end of the exposure period, the specimens were removed from the solution, surface-dried with a damp cloth, and oven-dried at 105 ± 5 °C until a constant mass was achieved. The final mass (W_1) was then recorded, and the percentage mass loss was calculated using the following Equation (2):

$$\text{Mass loss } (\%) = \frac{\text{Wo} - \text{W}_1}{\text{Wo}} \times 100 \quad (2)$$

where W_0 is the initial dry mass (g) and W_1 is the final dry mass after sulfate exposure (g). Three replicate specimens of 50 × 50 × 50 mm were tested for each mixture, and the average value was reported.

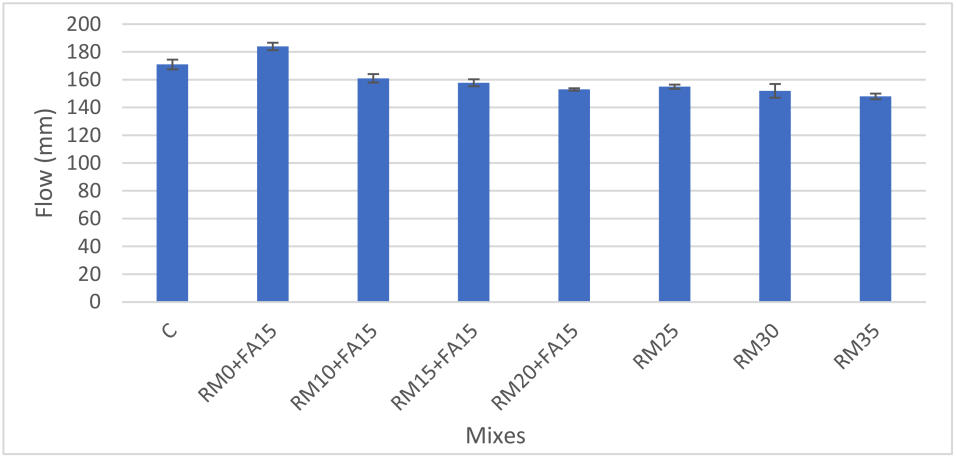
3.3.5. Scanning Electron Microscopy (SEM)

Microstructural analysis was performed using SEM to investigate the internal morphology, pore structure, and interfacial characteristics of selected mortar specimens. Small representative fragments were extracted from hardened specimens at the end of the curing period using a diamond saw. The samples were oven-dried to remove free moisture, and their surfaces were prepared prior to examination. SEM analysis was conducted to detect microcracks, unreacted particles, hydration products, and the quality of the interfacial transition zone (ITZ) between the cementitious matrix and the fiber and aggregate constituents.

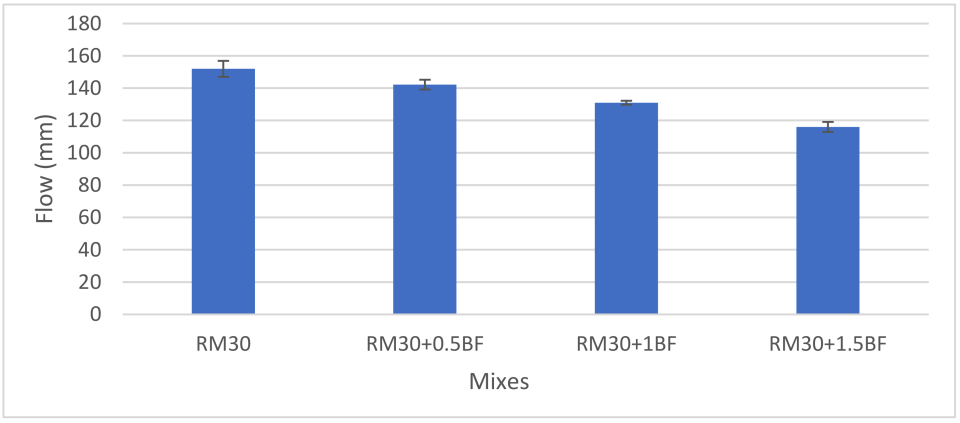
4. Results and Discussion

4.1. Flow Test

The fresh-state workability of all cement mortar mixtures was assessed using the flow test, and the results are presented in Figure 7a–c. As illustrated in Figure 7a, the incorporation of 15% FA without RM (RM0 + FA15) increased the flow value from 171 mm for the control mix (C) to 184 mm, representing an improvement of approximately 7.6%. This enhancement is attributed to the spherical particle morphology of Class F fly ash, which acts as miniature ball bearings within the fresh matrix, reducing inter-particle friction and water demand [50,51]. This effect is consistent with the physical characteristics of the FA used in this study, which exhibits a specific surface area of 345–380 m^2/kg and a smooth spherical particle morphology (Table 3). The combination of low surface roughness and near-uniform spherical geometry is understood to reduce contact-point friction between solid particles under shear, allowing particles to roll rather than interlock, thereby lowering the yield stress of the fresh mixture and increasing flow spread [50,51]. However, the progressive incorporation of RM alongside FA resulted in a systematic reduction in flow. The flow values decreased to 161 mm, 157.8 mm, and 153 mm at RM replacement levels of 10%, 15%, and 20% by weight of total binder, respectively. These results indicate that increasing the RM content adversely affected the workability of the fresh mortar mixtures. For mixtures containing RM as the sole partial cement replacement, a more pronounced reduction was observed, with flow values of 155 mm, 152 mm, and 148 mm recorded at RM contents of 25%, 30%, and 35%, respectively, confirming the progressive decline in fresh-state workability with increasing RM replacement.

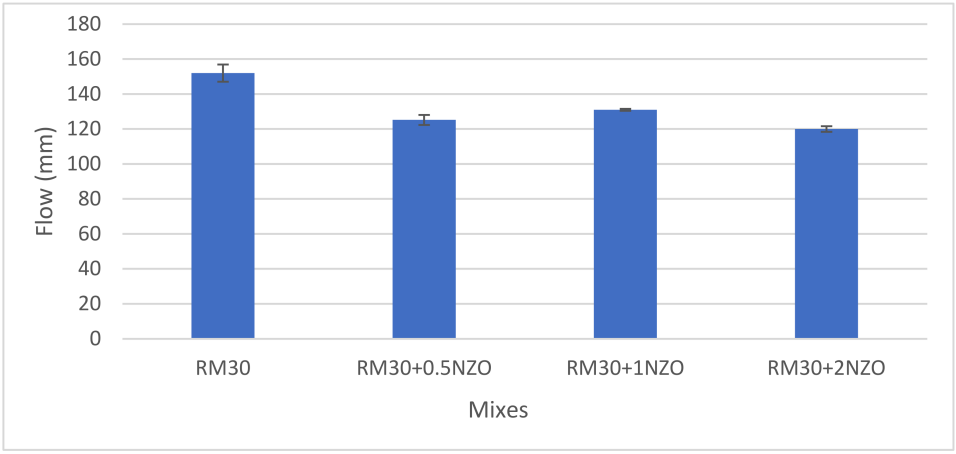


(**a**)



(**b**)

Figure 7. *Cont.*



(**c**)

Figure 7. Flow values of mixtures: (**a**) effect of RM and FA content, (**b**) effect of BF content on RM30 mixtures, and (**c**) effect of NZO content on RM30 mixtures.

The effect of basalt fiber addition on the flow of RM30 mixtures is presented in Figure 7b. The incorporation of BF resulted in a progressive reduction in flowability. Flow values declined from 152 mm for the unreinforced RM30 mixture to 142.2 mm, 131 mm, and 116 mm at BF contents of 0.5%, 1.0%, and 1.5%, respectively. This trend is consistent with fiber-reinforced mortar systems, where fibers act as physical obstructions that restrict particle mobility, increase internal friction, and promote mechanical interlocking within the fresh mix. The influence of NZO on the flow of RM30 mixtures is shown in Figure 7c. The addition of NZO generally reduced flowability compared with the reference RM30 mixture (152 mm). Flow values of 125.2 mm, 131 mm, and 120 mm were recorded at NZO contents of 0.5%, 1.0%, and 2.0%, respectively. The overall reduction is mainly attributed to the ultrafine particle size and high specific surface area of NZO, which increase water demand and enhance matrix cohesion [35,41]. The slightly higher flow observed at 1.0% NZO compared with 0.5% NZO may be related to improved particle packing and more efficient nanoparticle dispersion at this dosage [52]. At 2.0% NZO, particle agglomeration likely offsets any beneficial dispersion effects, resulting in the lowest flow value of 120 mm among the NZO series.

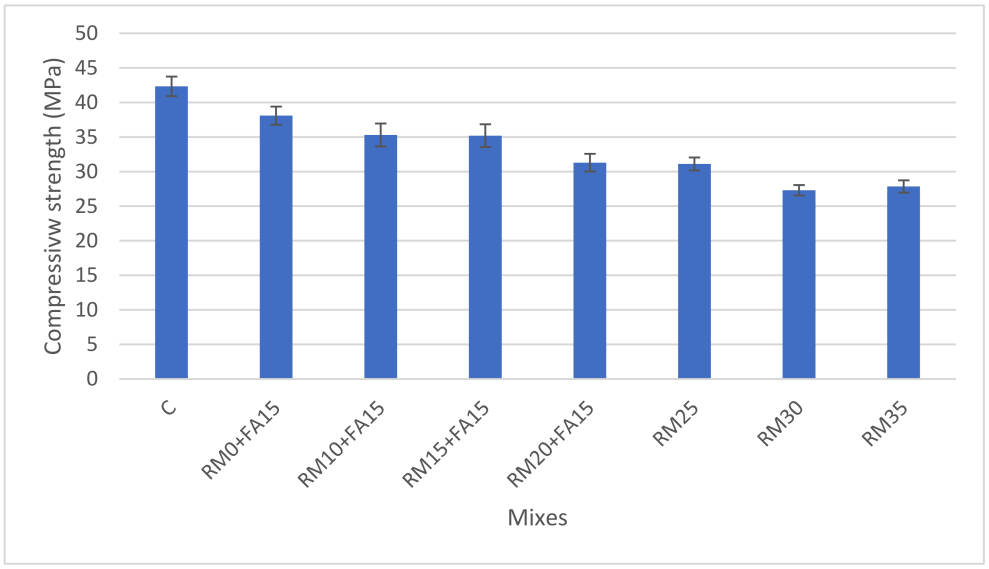
4.2. Compressive Strength

Compressive strength is one of the most critical mechanical properties of cement mortar, as it reflects the degree of hydration, matrix densification, and the quality of the interfacial transition zone. The 28-day compressive strength results of all investigated mixtures incorporating varying proportions of RM, FA, BF, and nano zinc oxide (NZO) are presented in Figure 8a–c. As shown in Figure 8a, the incorporation of 15% FA as partial binder replacement (RM0 + FA15) reduced the compressive strength from 42.32 MPa for the control mix (C) to 38.1 MPa, corresponding to a reduction of approximately 10%. This reduction is mainly attributed to the relatively slow pozzolanic reaction of FA at early curing ages, which delays the formation of calcium silicate hydrate (C–S–H) responsible for strength development. When RM was incorporated together with 15% FA at replacement levels of 10%, 15%, and 20% by weight of total binder, the compressive strengths decreased to 35.3, 35.2, and 31.3 MPa, respectively, representing reductions of approximately 16.5%, 16.8%, and 26.1% compared with the control mix. This decline is primarily associated with cement dilution and the comparatively lower hydraulic reactivity of RM at early ages. The high iron oxide content and crystalline phases in RM retard hydration reactions and result in less compact reaction products. Notably, the compressive strength of RM25

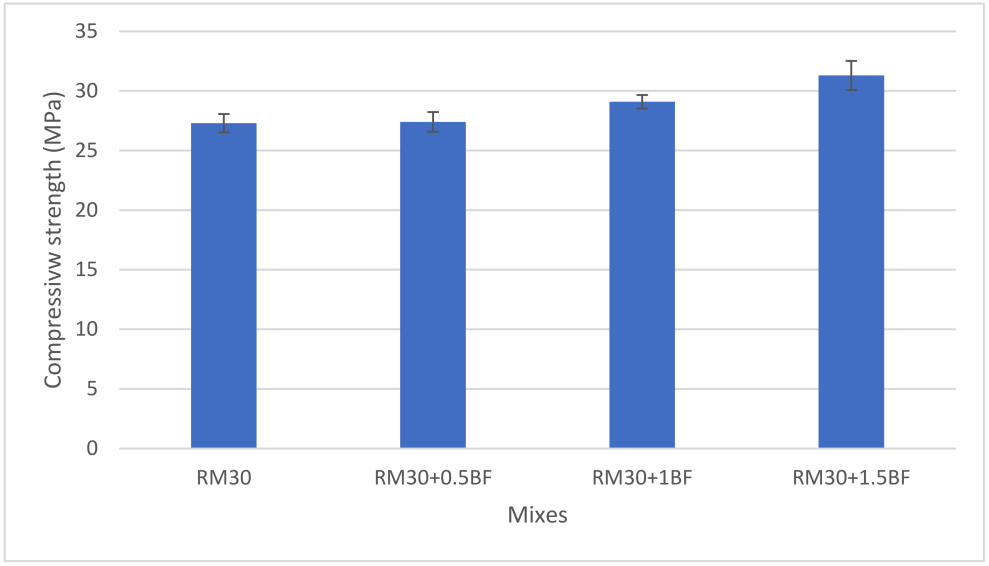
(31.11 MPa) was comparable to that of RM20 + FA15 (31.3 MPa), suggesting that the pozzolanic contribution of FA partially compensates for the strength reduction associated with higher RM replacement levels. Tukey HSD confirms no significant difference between these two mixtures (q = 0.26, p = 1.00).

The influence of RM as a sole partial cement replacement without FA is also illustrated in Figure 8a. A pronounced reduction in compressive strength was observed with increasing RM content. Compared with the control mix, compressive strengths of 31.11, 27.3, and 27.85 MPa were recorded at RM replacement levels of 25%, 30%, and 35% by weight of total binder, corresponding to reductions of approximately 26.5%, 35.5%, and 34.2%, respectively. The compressive strength recorded for RM35 (27.85 MPa) was statistically indistinguishable from RM30 (27.3 MPa) (Tukey HSD, q = 0.75, p = 1.00), indicating that additional RM beyond 30% replacement neither improves nor further reduces compressive strength within this dataset. The slightly higher compressive strength recorded for RM35 (27.85 MPa) compared with RM30 (27.3 MPa) may be attributed to the micro-filler effect of additional RM particles, which partially densify the matrix despite their limited hydraulic reactivity. The effect of basalt fiber addition on RM30 mixtures is presented in Figure 8b. A progressive enhancement in compressive strength was observed with increasing BF content. The incorporation of 0.5%, 1.0%, and 1.5% BF increased compressive strength from 27.3 MPa for the unreinforced RM30 mixture to 27.4, 29.1, and 31.3 MPa, corresponding to improvements of approximately 0.4%, 6.6%, and 14.7%, respectively. This improvement is attributed to the micro-reinforcement mechanism of basalt fibers, which bridge microcracks, delay crack propagation, and improve stress transfer within the cementitious matrix. Tukey HSD post hoc testing indicates that only the 1.0% and 1.5% BF dosages produced statistically significant compressive-strength gains relative to RM30 ($p < 0.05$); the 0.4% increase recorded at 0.5% BF was not statistically significant (q = 0.14, p = 1.00) and should be interpreted as measurement variability rather than a genuine strengthening effect. Although basalt fibers demonstrated significant mechanical improvements within the 28-day testing scope, their long-term durability in the high-alkalinity red mud matrix (pH ≈ 12–13, Na_2O ~10.83%) requires further consideration. The Si–O–Si bonds within the basalt fiber silicate framework can react with OH^- ions, causing surface pitting corrosion and progressive strength degradation over extended periods [53]. Therefore, the crack-bridging benefits reported herein should be interpreted within the short-term curing context, and long-term fiber–matrix interfacial durability in red mud-based systems warrants dedicated alkali-accelerated aging investigation.

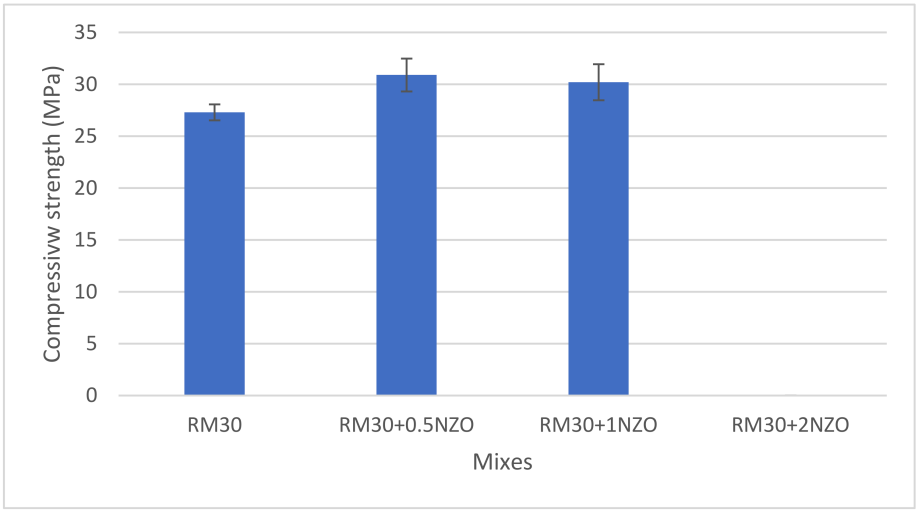
The influence of NZO on RM30 mixtures is shown in Figure 8c. However, increasing NZO content to 2.0% resulted in a complete loss of compressive strength. This catastrophic decline is governed by three sequential and mutually reinforcing mechanisms. First, at this elevated dosage, the high surface energy of NZO nanoparticles promotes severe agglomeration rather than uniform dispersion; these agglomerates act as discrete flaws within the matrix, concentrating stress and initiating premature cracking under load rather than contributing to pore refinement. Second, dissolved Zn^{2+} ions are well documented to retard cement hydration by adsorbing onto clinker surfaces and forming a zinc hydroxide ($Zn(OH)_2$) barrier layer. The combined effect of agglomeration-induced stress concentration, hydration retardation, and non-cementitious phase formation therefore explains why the detrimental mechanisms at 2.0% NZO overwhelm the beneficial nano-filler and nucleation effects observed at lower dosages, resulting in the observed strength collapse [35,39].



(**a**)



(**b**)



(**c**)

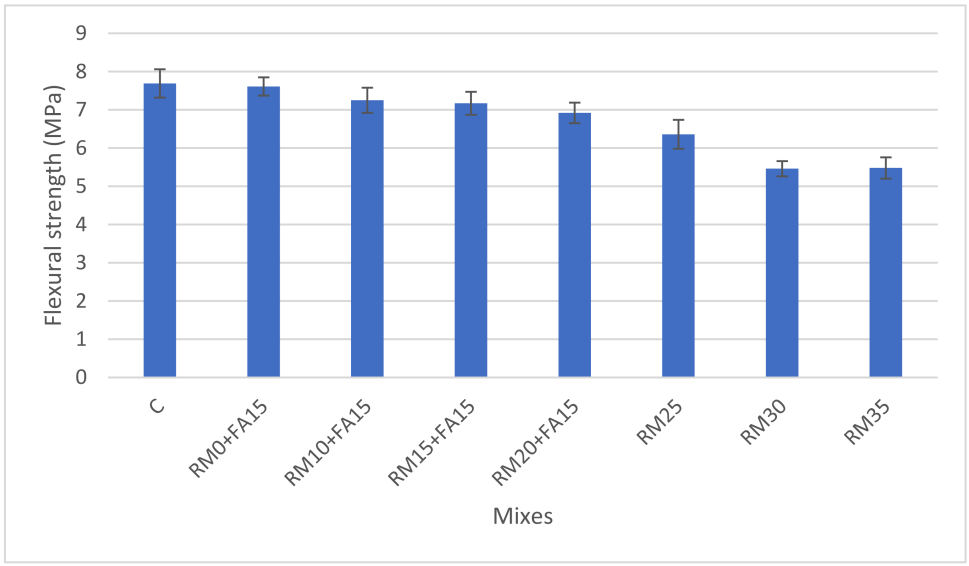
Figure 8. Compressive strength of cement mortar mixtures: (**a**) effect of RM and FA content, (**b**) effect of BF content on RM30 mixtures, and (**c**) effect of NZO content on RM30 mixtures.

4.3. Flexural Strength

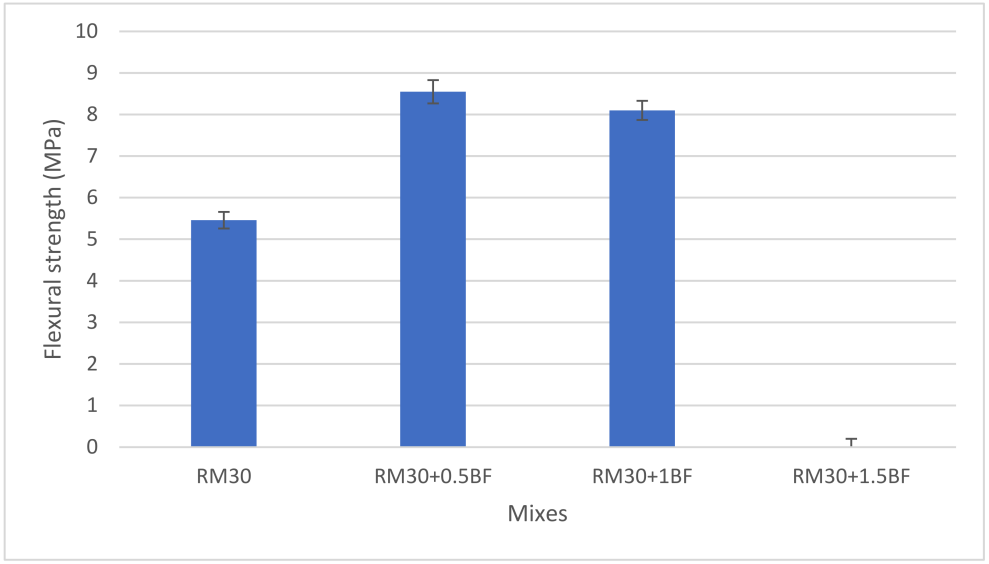
Flexural strength reflects the ability of cement mortar to resist tensile stresses induced under bending loads and is closely related to the quality of the interfacial transition zone, matrix porosity, and fiber reinforcement. The 28-day flexural strength results of all investigated mixtures are presented in Figure 9a–c. As shown in Figure 9a, the incorporation of 15% FA as partial binder replacement (RM0 + FA15) resulted in a marginal reduction in flexural strength from 7.69 MPa for the control mix (C) to 7.61 MPa, corresponding to a reduction of less than 1.0%. This minimal reduction can be attributed to the filler effect and the delayed pozzolanic reaction of FA, which contribute to matrix densification and improved resistance to crack initiation at later curing stages [54,55].

When RM was incorporated together with 15% FA at replacement levels of 10%, 15%, and 20% by weight of total binder, the flexural strengths decreased to 7.25, 7.17, and 6.92 MPa, representing reductions of approximately 5.7%, 6.7%, and 10.0%, respectively, compared with the control mix. This gradual decrease is mainly associated with the dilution of reactive cementitious phases and the limited tensile contribution of RM particles, which reduces resistance to crack propagation under bending stresses. The behavior of RM as a sole cement replacement without FA is also illustrated in Figure 9a. A more pronounced decrease in flexural strength was observed with increasing RM content. Compared with the control mix, flexural strengths of 6.36, 5.46, and 5.48 MPa were recorded at RM replacement levels of 25%, 30%, and 35%, corresponding to reductions of approximately 17.3%, 29.0%, and 28.7%, respectively. The flexural strength of RM35 (5.48 MPa) was statistically indistinguishable from RM30 (5.46 MPa) (Tukey HSD, q = 0.12, p = 1.00), indicating no genuine mechanical difference between these two RM-only mixtures. The slightly higher flexural strength of RM35 (5.48 MPa) compared with RM30 (5.46 MPa) may similarly be attributed to factors discussed previously (Section 4.2).

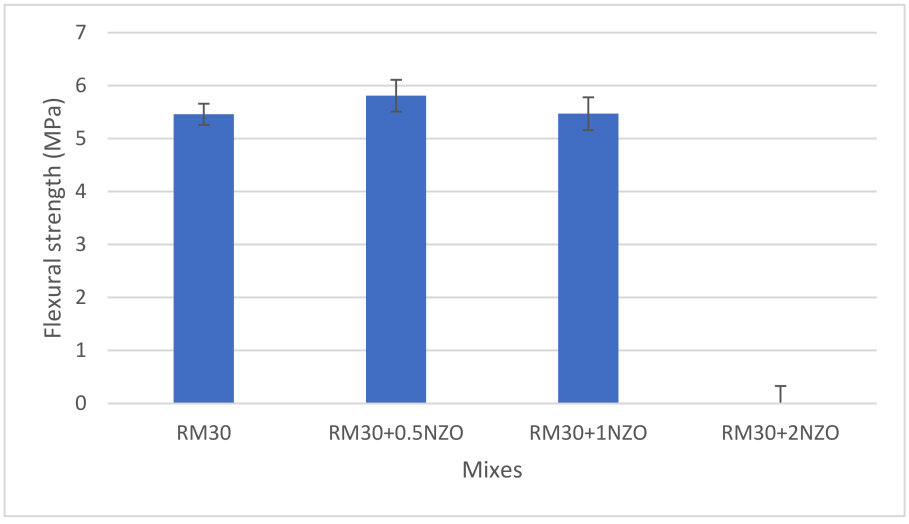
The influence of BF on the flexural performance of RM30 mixtures is presented in Figure 9b. A substantial and progressive enhancement in flexural strength was observed with increasing BF content. The incorporation of 0.5%, 1.0%, and 1.5% BF increased flexural strength from 5.46 MPa for the unreinforced RM30 mixture to 6.35, 6.6, and 7.51 MPa, corresponding to improvements of approximately 16.3%, 20.9%, and 37.5%, respectively. This significant enhancement is primarily attributed to the crack-bridging mechanism of basalt fibers, fiber pull-out resistance, and improved stress transfer along microcracks under bending loads. The influence of NZO on the flexural strength of RM30 mixtures is shown in Figure 9c. The addition of NZO at low dosages significantly improved flexural strength. Compared with the RM30 reference mix (5.46 MPa), flexural strengths of 6.46 and 6.20 MPa were recorded at 0.5% and 1.0% NZO, corresponding to improvements of approximately 18.3% and 13.5%, respectively. These improvements are attributed to the nano-filler and nucleation effects of NZO, which refine pore structure and enhance matrix densification [35,56]. Consistent with the compressive strength results, the optimal NZO content for flexural performance was 0.5%. At a higher dosage of 2.0%, flexural strength reduced significantly. A dedicated one-way ANOVA within the NZO series (RM30, 0.5%, and 1.0% NZO) confirms a significant overall effect on flexural strength ($F(2,6) = 9.9$, p = 0.013), but Tukey HSD shows 0.5% and 1.0% NZO are not significantly different from each other on flexural strength (q = 1.54, p = 0.995) or compressive strength (q = 0.95, p = 1.00); both dosages clearly outperform RM30 alone, but "0.5% NZO is optimal" is only statistically distinguishable from 1.0% NZO for sulfate mass loss (p = 0.007), not for strength.



(**a**)



(**b**)



(**c**)

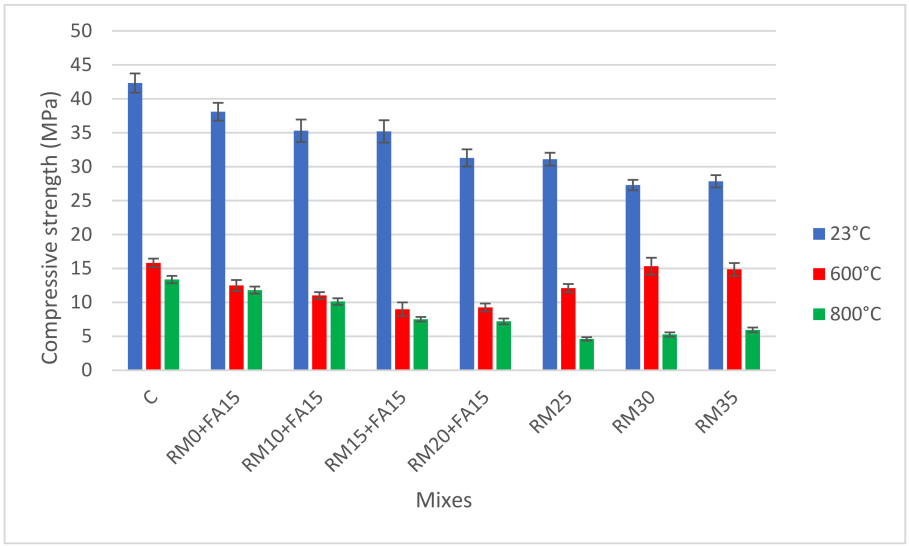
Figure 9. Flexural strength of cement mortar mixtures: (**a**) effect of RM and FA content, (**b**) effect of BF content on RM30 mixtures, and (**c**) effect of NZO content on RM30 mixtures.

4.4. Residual Mechanical Properties After Elevated Temperature Exposure

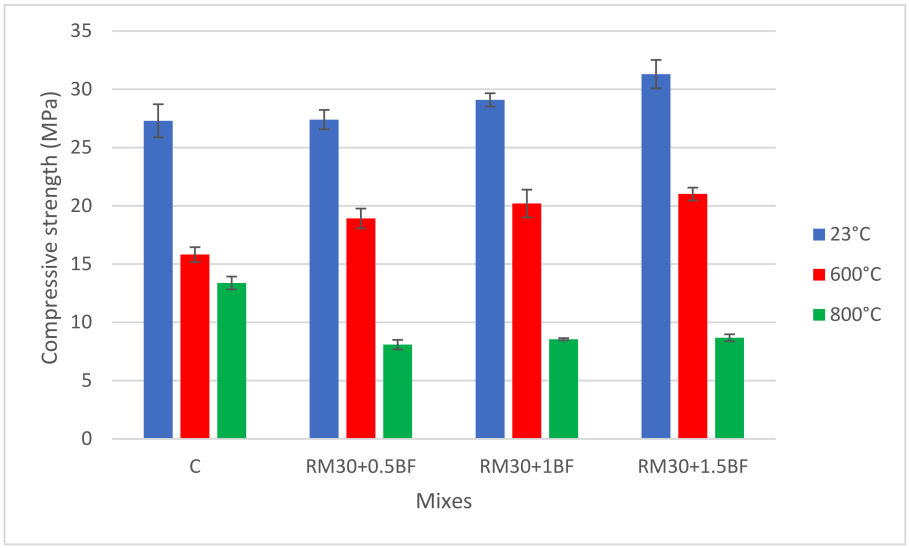
4.4.1. Compressive Strength

The residual compressive strength of all mortar mixtures after exposure to elevated temperatures of 600 °C and 800 °C for one hour is presented in Figure 10a–c. All mixtures experienced significant strength degradation with increasing temperature, reflecting the progressive decomposition of hydration products and thermally induced microcracking within the cementitious matrix. As shown in Figure 10a, the control mix (C) exhibited residual compressive strengths of 15.82 and 13.38 MPa at 600 °C and 800 °C, respectively, corresponding to reductions of approximately 62.6% and 68.4% relative to its 28-day ambient strength.

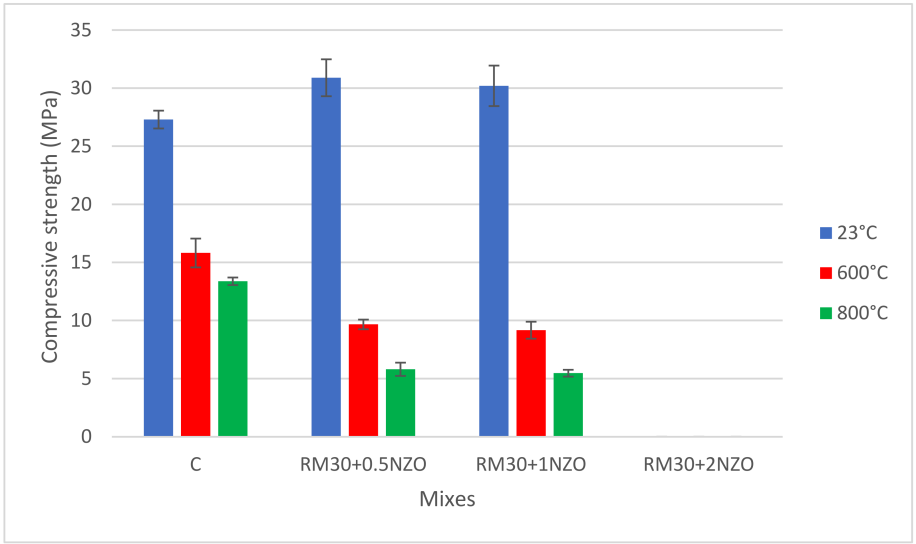
The incorporation of 15% FA (RM0 + FA15) resulted in greater strength reductions, with residual strengths of 12.5 and 11.82 MPa at 600 °C and 800 °C, corresponding to reductions of approximately 67.2% and 69.0%. This increased susceptibility is attributed to the decomposition of FA-derived C–S–H at elevated temperatures and the inherent sensitivity of aluminosilicate gel products to thermal degradation [54,56]. When RM was incorporated together with 15% FA, residual compressive strength decreased progressively with increasing RM content. At 600 °C, strengths of 11.04, 9.0, and 9.26 MPa were recorded for RM10 + FA15, RM15 + FA15, and RM20 + FA15 mixtures, respectively. At 800 °C, corresponding strengths of 10.14, 7.53, and 7.22 MPa were obtained, representing reductions of approximately 71.3–78.6% relative to ambient strength. The residual compressive strength of RM-only mixtures is also illustrated in Figure 10a. Notably, RM-only mixtures demonstrated relatively improved residual strength at 600 °C compared with RM–FA blends. RM25, RM30, and RM35 recorded residual strengths of 12.11, 15.35, and 14.87 MPa at 600 °C, respectively. The superior thermal performance of RM30 and RM35 at 600 °C, despite their lower ambient strength, may be attributed to the high iron oxide content of RM (Fe_2O_3 = 23.79%), which promotes the formation of thermally stable crystalline phases at intermediate temperatures [57]. However, at 800 °C, severe deterioration occurred in RM-only mixtures, with residual strengths dropping to 4.63, 5.29, and 5.95 MPa for RM25, RM30, and RM35, respectively, corresponding to reductions of approximately 78.6–85.1%. Beyond 700–750 °C, however, this stabilizing mechanism reverses: iron oxide phases undergo further destabilizing transformations, which may be related to Na_2O-induced formation of low-melting-point phases at elevated temperatures, proposed by analogy with [57–60] rather than directly observed via mineralogical analysis in this study. This confirms that the beneficial contribution of iron oxide-rich phases in RM is temperature-dependent and insufficient as a standalone thermal resistance mechanism under severe fire exposure conditions. The influence of BF on the residual compressive strength of RM30 mixtures after elevated temperature exposure is presented in Figure 10b. Basalt fiber-reinforced mixtures demonstrated significantly enhanced thermal performance compared with the unreinforced RM30 mix. Residual compressive strengths of 18.92, 20.2, and 21.02 MPa were recorded at 600 °C for RM30 + 0.5BF, RM30 + 1BF, and RM30 + 1.5BF, respectively, representing improvements of approximately 23.3%, 31.7%, and 37.0% over the unreinforced RM30 mixture at the same temperature. At 800 °C, residual strengths of 8.1, 8.55, and 8.68 MPa were obtained, confirming the sustained crack-bridging action and thermal stability of basalt fibers at elevated temperatures.



(**a**)



(**b**)



(**c**)

Figure 10. Residual compressive strength of cement mortar mixtures at 600 °C and at 800 °C: (**a**) effect of RM and FA content, (**b**) effect of BF content on RM30 mixtures, and (**c**) effect of NZO content on RM30 mixtures.

The influence of NZO on the residual compressive strength of RM30 mixtures is shown in Figure 10c. In contrast to BF, the incorporation of NZO adversely affected thermal performance. Residual compressive strengths of 9.67 and 9.17 MPa were recorded at 600 °C for RM30 + 0.5NZO and RM30 + 1NZO, respectively, representing reductions of approximately 37% and 40% compared with the unreinforced RM30 mixture at 600 °C, and reductions of 68.7% and 69.6% relative to their respective ambient strengths. At 800 °C, residual strengths of 5.81 and 5.47 MPa were obtained, corresponding to reductions of about 81–82%. The RM30 + 2NZO mixture recorded zero residual strength at both temperatures, consistent with its complete strength loss at ambient conditions. The poor thermal performance of NZO-modified mixtures is attributed to nanoparticle agglomeration, matrix densification, and restricted vapor release leading to internal pressure accumulation and explosive spalling [56,61]. Furthermore, NZO-modified specimens exhibited severe deterioration after heating and, in some cases, explosive spalling occurred, preventing accurate determination of residual strength. This behavior is linked to matrix densification caused by NZO, which restricts vapor escape during heating and leads to rapid pore pressure build-up and structural failure [56,61].

The visual appearance of mortar specimens after exposure to elevated temperatures is presented in Figure 11. A noticeable color transformation from gray to reddish-brown was observed with increasing temperature, accompanied by the progressive development of surface cracking and structural deterioration. The color shift is associated with dehydration of hydration products, oxidation of iron-bearing phases present in red mud, and crystalline phase transformations within the cementitious matrix [59,60].



Figure 11. Visual appearance of cement mortar specimens after exposure to elevated temperatures, showing color transformation and surface cracking.

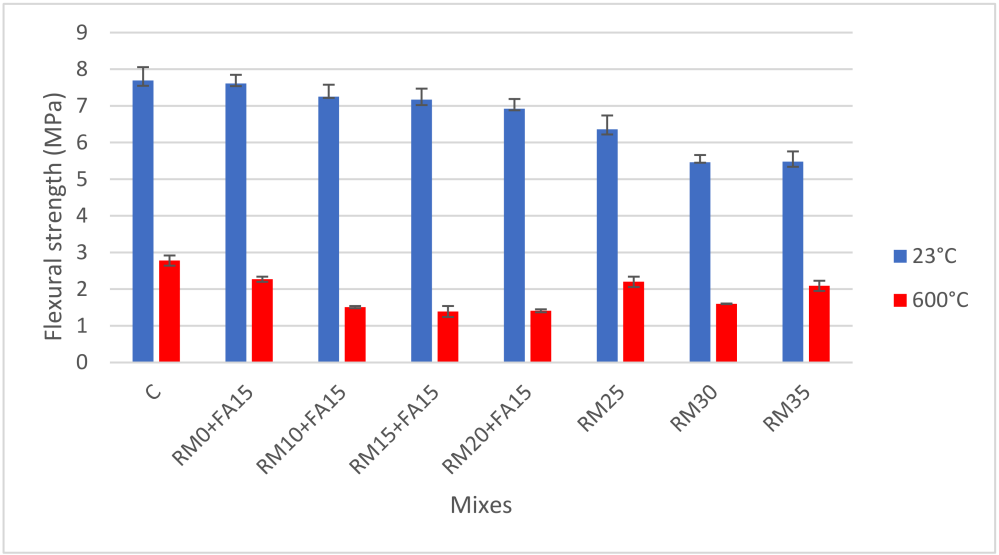
4.4.2. Flexural Strength

The residual flexural strength of all mortar mixtures after exposure to 600 °C for one hour is presented in Figure 12a–c. All mixtures experienced significant reductions in flexural strength, reflecting the progressive decomposition of hydration products, microcrack formation, and bond degradation under thermal loading [59,60].

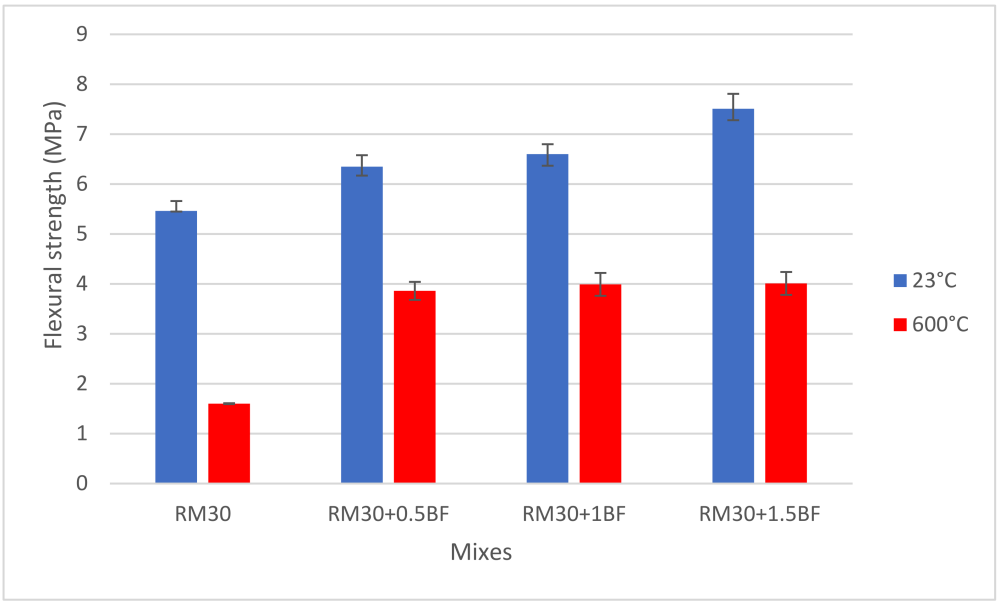
As shown in Figure 12a, the control mix (C) exhibited a residual flexural strength of 2.78 MPa after exposure to 600 °C, corresponding to a reduction of approximately 63.8% relative to its 28-day ambient strength. The incorporation of 15% FA (RM0 + FA15) resulted in a greater reduction, with a residual flexural strength of 2.27 MPa, corresponding to a reduction of approximately 70.2%. When RM was incorporated together with 15% FA, residual flexural strengths decreased progressively with increasing RM content, recording 1.51, 1.39, and 1.41 MPa for RM10 + FA15, RM15 + FA15, and RM20 + FA15, respectively, representing reductions of approximately 79.2%, 80.6%, and 79.6% relative to ambient strength. This behavior is associated with cement dilution, reduced tensile load-carrying capacity, and thermal instability of RM-rich matrices. Notably, RM-only mixtures demonstrated relatively improved residual flexural performance compared with RM–FA blends. RM25, RM30, and RM35 recorded residual flexural strengths of 2.2, 1.6, and 2.09 MPa, respectively, corresponding to reductions of approximately 65.4%, 70.7%, and 61.9%. The slightly higher residual flexural strength of RM35 (2.09 MPa) compared with RM30 (1.6 MPa) may be attributed to factors discussed previously (Section 4.2), enhancing intermediate-temperature stability [58,62]. The effect of BF addition on residual flexural strength at 600 °C is presented in Figure 12b. The incorporation of BF significantly reduced flexural strength loss compared with the unreinforced RM30 mixture (1.6 MPa). Residual flexural strengths of 3.86, 3.99, and 4.01 MPa were recorded for RM30 + 0.5BF, RM30 + 1BF, and RM30 + 1.5BF, respectively, corresponding to reductions of approximately 39.2%, 39.5%, and 46.6% relative to their ambient strengths. The improved thermal performance is attributed to the crack-bridging capability of BF, enhanced stress redistribution, and the inherent thermal stability of basalt fibers at elevated temperatures.

The influence of NZO on residual flexural strength at 600 °C is shown in Figure 12c. In contrast to BF, NZO-modified mixtures exhibited substantial deterioration after heating. Residual flexural strengths of 1.82 and 1.67 MPa were recorded for RM30 + 0.5NZO and RM30 + 1NZO, respectively, corresponding to reductions of approximately 71.8% and 73.1% relative to ambient strength. The RM30 + 2NZO mixture recorded zero residual flexural strength at 600 °C, consistent with its complete strength loss at ambient conditions. In some cases, explosive spalling occurred, preventing accurate determination of residual flexural strength.

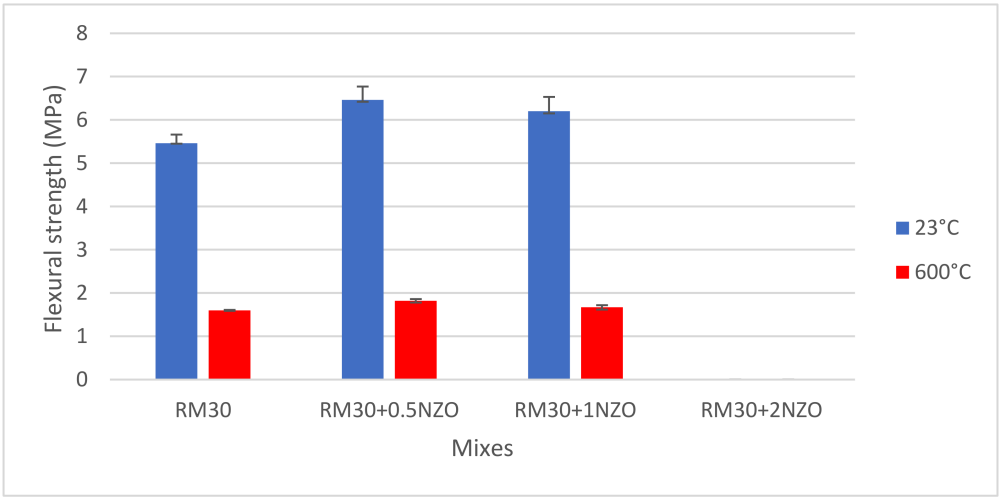
The residual flexural strength data demonstrate that BF-reinforced mixtures exhibited the lowest strength reduction at 600 °C among all modified systems, while NZO-modified mixtures showed the most severe deterioration, particularly at dosages exceeding the optimal threshold where vapor pressure accumulation led to explosive spalling and complete strength loss.



(**a**)



(**b**)



(**c**)

Figure 12. Residual flexural strength of cement mortar mixtures at 600 °C: (**a**) effect of RM and FA content, (**b**) effect of BF content on RM30 mixtures, and (**c**) effect of NZO content on RM30 mixtures.

4.5. Sulfate Resistance

The mass loss of all mortar specimens after 28 days of immersion in a 5% sodium sulfate solution is presented in Figure 13.

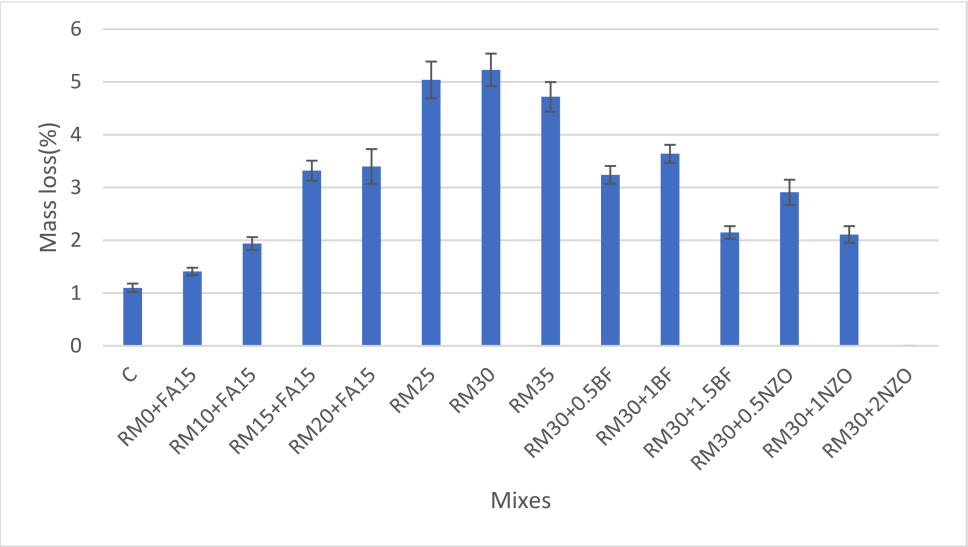


Figure 13. Mass loss (%) of RM-based mortar mixes immersed in 5% Na_2SO_4 solution. Note: The zero-mass loss recorded for RM30 + 2NZO does not indicate improved sulfate resistance; this specimen disintegrated completely during immersion, preventing accurate mass loss determination, and should not be compared directly with other mixtures.

As shown in Figure 13, the control mix (C) exhibited the lowest mass loss of 1.1%, reflecting the relatively dense and stable microstructure of plain cement mortar. The incorporation of 15% FA (RM0 + FA15) resulted in a slightly higher mass loss of 1.41%. When RM was incorporated together with 15% FA, mass loss increased progressively with increasing RM content, recording 1.94%, 3.32%, and 3.4% for RM10 + FA15, RM15 + FA15, and RM20 + FA15, respectively. This trend suggests that higher RM levels combined with FA accelerate sulfate-induced deterioration due to increased reactive alumina and iron-rich phases that facilitate the formation of expansive ettringite [63]. RM-only mixtures exhibited higher mass loss compared with RM–FA blends, with values of 5.04%, 5.23%, and 4.72% recorded for RM25, RM30, and RM35, respectively. The increased susceptibility of RM-only mixtures is attributed to the high alkalinity of RM, its relatively porous microstructure, and the presence of soluble sodium compounds that facilitate sulfate ingress and leaching [62–64]. The slightly lower mass loss of RM35 (4.72%) compared with RM30 (5.23%) may be attributed to the factors discussed previously (Section 4.2). The mass loss of RM35 (4.72%) was not statistically distinguishable from RM30 (5.23%) (Tukey HSD, q = 4.04, $p = 0.24$), so this difference should not be interpreted as a genuine densification effect.

The incorporation of BF improved sulfate resistance compared with the unreinforced RM30 mixture (5.23%), as shown in Figure 13. Mass loss values of 3.24%, 3.64%, and 2.15% were recorded for RM30 + 0.5BF, RM30 + 1BF, and RM30 + 1.5BF, respectively. The optimal performance was achieved at 1.5% BF, with a mass loss of 2.15%, representing a reduction of approximately 58.9% compared with the unreinforced RM30 mixture. This enhancement is mainly attributed to the crack-bridging action of BF, which limits microcrack propagation and reduces sulfate ion penetration into the matrix. This claim is supported by dedicated within-series testing: the BF-series ANOVA on mass loss is significant ($F(3,8) = 116.1$, $p < 0.001$), and Tukey HSD confirms 1.5% BF is significantly better than both 1.0% BF ($p < 0.001$) and 0.5% BF for this property, unlike the compressive-strength version of the 1.5–BF claim, which is only directionally, not statistically, distinct from 1.0% BF.

The incorporation of NZO at low dosages also improved sulfate resistance, as shown in Figure 13. Mass loss values of 2.91% and 2.11% were recorded for RM30 + 0.5NZO and RM30 + 1NZO, respectively, representing reductions of approximately 44.4% and 59.7% compared with the unreinforced RM30 mixture. These improvements are attributed to the nano-filler and nucleation effects of NZO, which refine pore structure, reduce permeability, and limit sulfate ion diffusion into the matrix [35,56]. The RM30 + 2NZO mixture recorded a mass loss of 0%, not due to improved sulfate resistance, but because the specimen disintegrated completely during immersion, preventing accurate mass loss determination. This catastrophic deterioration is consistent with the complete mechanical strength loss observed in RM30 + 2NZO at ambient conditions, and reflects the severe matrix disruption caused by excessive NZO dosage [35,39,61]. Table 8 presents a comprehensive summary of all experimental results.

Table 8. Experimental results (Mean ± SD) of all mortar mixtures.

Mixture	Flow (mm)	fcu 23 °C (MPa)	fcu 600 °C (MPa)	fcu 800 °C (MPa)	Flexural Strength 23 °C (MPa)	Flexural Strength 600 °C (MPa)	Mass Loss (%)
C	171.0 ± 3.49	42.32 ± 1.42	15.82 ± 0.64	13.38 ± 0.55	7.69 ± 0.37	2.78 ± 0.14	1.10 ± 0.08
RM0 + FA15	184.0 ± 2.67	38.10 ± 1.31	12.50 ± 0.82	11.82 ± 0.53	7.61 ± 0.24	2.27 ± 0.07	1.41 ± 0.07
RM10 + FA15	161.0 ± 3.06	35.30 ± 1.66	11.04 ± 0.49	10.14 ± 0.49	7.25 ± 0.33	1.51 ± 0.03	1.94 ± 0.12
RM15 + FA15	157.8 ± 2.51	35.20 ± 1.65	9.00 ± 1.01	7.53 ± 0.33	7.17 ± 0.3	1.39 ± 0.15	3.32 ± 0.19
RM20 + FA15	153.0 ± 0.88	31.30 ± 1.27	9.26 ± 0.59	7.22 ± 0.42	6.92 ± 0.27	1.41 ± 0.04	3.40 ± 0.33
RM25	155.0 ± 1.53	31.11 ± 0.94	12.11 ± 0.61	4.63 ± 0.25	6.36 ± 0.38	2.20 ± 0.14	5.04 ± 0.35
RM30	152.0 ± 4.96	27.30 ± 0.77	15.35 ± 1.24	5.29 ± 0.32	5.46 ± 0.2	1.60 ± 0.01	5.23 ± 0.31
RM35	148.0 ± 1.99	27.85 ± 0.90	14.87 ± 0.94	5.95 ± 0.36	5.48 ± 0.28	2.09 ± 0.14	4.72 ± 0.28
RM30 + 0.5BF	142.2 ± 2.99	27.40 ± 0.83	18.92 ± 0.85	8.10 ± 0.41	6.35 ± 0.23	3.86 ± 0.18	3.24 ± 0.17
RM30 + 1BF	131.0 ± 1.26	29.10 ± 0.57	20.20 ± 1.19	8.55 ± 0.1	6.60 ± 0.2	3.99 ± 0.23	3.64 ± 0.17
RM30 + 1.5BF	116.0 ± 3.11	31.30 ± 1.22	21.02 ± 0.55	8.68 ± 0.30	7.51 ± 0.3	4.01 ± 0.23	2.15 ± 0.12
RM30 + 0.5NZO	125.2 ± 2.87	30.90 ± 1.59	9.67 ± 0.42	5.81 ± 0.57	6.46 ± 0.31	1.82 ± 0.04	2.91 ± 0.24
RM30 + 1NZO	131.0 ± 0.59	30.20 ± 1.74	9.17 ± 0.73	5.47 ± 0.29	6.20 ± 0.33	1.67 ± 0.05	2.11 ± 0.16
RM30 + 2NZO	120.0 ± 1.62	-	-	-	-	-	-

Note: The RM30 + 2NZO mixture completely disintegrated during immersion, preventing accurate determination of its results, and should not be directly compared to other mixtures. Its exclusion reflects complete mechanical failure rather than missing-at-random data; consequently, the ANOVA and post hoc comparisons reported in Section 6 describe the thirteen surviving mixtures only and should not be interpreted as unbiased estimates inclusive of RM30 + 2NZO's true (zero) performance.

4.6. Statistical Analysis and Reproducibility of Experimental Data

The reproducibility and statistical significance of the experimental data were evaluated through standard deviation (SD) analysis and one-way analysis of variance (ANOVA), with results summarized in Tables 8 and 9, respectively. The SD values recorded across all mixtures and properties were consistently low, reflecting high reproducibility of the experimental program. Average SD values of 2.45 mm, 1.22 MPa, 0.78 MPa, 0.38 MPa, 0.29 MPa, 0.11 MPa, and 0.20% were recorded for flow, compressive strength at 23 °C, residual compressive strength at 600 °C and 800 °C, flexural strength at 23 °C, residual flexural strength at 600 °C, and mass loss, respectively, corresponding to average coefficients of variation (CV) of 1.66%, 3.78%, 5.96%, 5.06%, 4.34%, 4.54%, and 6.42%. These CV values are within the acceptable range reported for cementitious composite testing, confirming the consistency and reliability of the replicate specimens. Furthermore, one-way ANOVA confirmed that mixture type had a statistically significant effect on all measured properties ($p < 0.001$), with F-statistics of 147.66, 36.85, 83.05, 130.97, 19.08, 168.99, and 112.41 for flow, compressive strength, residual compressive strength at 600 °C and 800 °C, flexural strength, residual flexural strength, and mass loss, respectively (df = 12, 26). These results confirm that the performance differences observed across the fourteen mortar mixtures

are statistically significant and cannot be attributed to random experimental variability, thereby validating the reliability of the reported findings.

Table 9. One-way ANOVA results and standard deviation analysis for fresh-state and mechanical properties of all investigated mortar mixtures (df between = 12, df within = 26; $\alpha = 0.05$).

Property	F-Statistic	Significance ($\alpha = 0.05$)	Interpretation
Flow (mm)	147.664	Yes	Mixture type has a statistically significant effect
fcu 23 °C (MPa)	36.846	Yes	Mixture type has a statistically significant effect
fcu 600 °C (MPa)	83.047	Yes	Mixture type has a statistically significant effect
fcu 800 °C (MPa)	130.971	Yes	Mixture type has a statistically significant effect
Flexural 23 °C (MPa)	19.081	Yes	Mixture type has a statistically significant effect
Flexural 600 °C (MPa)	168.992	Yes	Mixture type has a statistically significant effect
Mass Loss (%)	112.411	Yes	Mixture type has a statistically significant effect

Normality of residuals was assumed rather than formally tested; with only three replicates per mixture, distributional tests such as Shapiro–Wilk have negligible power and were not considered informative. Homogeneity of variance was assessed using Bartlett's test for each property: six of the seven properties showed no evidence of unequal variances (Bartlett $p > 0.5$), while residual flexural strength at 600 °C showed a significant violation (Bartlett statistic = 21.9, $p = 0.039$); Welch's F-test, which does not assume equal variances, confirmed the same conclusion for this property (Welch F = 155.6, $p < 0.001$). Applying a Bonferroni correction across the seven property-level ANOVAs (family-wise alpha = 0.05/7 = 0.00714) does not alter any conclusion, as all seven omnibus F-tests remain significant at $p < 10^{-9}$. All pairwise comparisons discussed narratively in this manuscript were tested using Tukey's HSD, which controls the family-wise error rate within each property's ANOVA. To evaluate constituent-specific effects beyond the global mixture-type factor, dedicated one-way ANOVAs were additionally performed within each constituent series (RM/FA, RM-only, BF, and NZO); all four series showed statistically significant within-series effects. Effect sizes (eta-squared), computed from the same sums of squares, ranged from 0.899 (flexural strength at 23 °C) to 0.987 (residual flexural strength at 600 °C) across all seven properties, indicating that mixture type accounts for the substantial majority of variance observed.

4.7. Scanning Electron Microscopy (SEM)

The microstructure of selected cement mortar mixtures was investigated using scanning electron microscopy (SEM) at various magnifications, as presented in Figure 14. The analysis focused on three mixtures incorporating 15% FA in combination with RM replacement levels of 10%, 15%, and 20% by weight of total binder.

As shown in Figure 14a, the RM10 + FA15 mixture exhibits a moderately developed cementitious matrix characterized by the coexistence of spherical FA particles and angular, plate-like RM fragments embedded within the hydrated cement paste. The spherical morphology of FA particles is clearly identifiable at this magnification, consistent with the ball-bearing effect attributed to FA in improving fresh-state workability [50,51]. Partial dissolution of FA particles is evident from eroded and roughened surface edges, indicating active participation in pozzolanic reactions and the initiation of secondary C–S–H gel formation. RM particles display rough, crystalline surfaces with relatively lower dissolution compared with FA, consistent with the limited hydraulic reactivity of RM at early curing ages and the dominance of crystalline iron- and alumina-bearing phases in its mineralogical composition [55,64]. The C–S–H gel network appears continuous but moderately dense, with thin gel coatings surrounding both FA and RM particles. The interfacial transition zone between RM particles and the cement paste matrix is moderately developed, with limited micro-cracking observed at the particle boundaries. Some inter-particle micro-voids are

visible, reflecting the incomplete densification associated with the relatively lower RM content at this replacement level. Despite this moderate porosity, the overall matrix integrity is maintained, which is consistent with the acceptable compressive and flexural strength values recorded for RM10 + FA15 at ambient temperature [65–67]. The microstructure of the RM15 + FA15 mixture, shown in Figure 14b, exhibits a more developed, compact, and homogeneous cementitious matrix compared with the RM10 + FA15 mixture. Thicker C–S–H gel layers and nano-scale gel clusters are clearly visible at higher magnifications, filling inter-particle voids and significantly enhancing matrix continuity and densification. The gel network appears well-developed and interconnected, with reaction products uniformly distributed throughout the matrix. Short plate-like crystalline phases are observed bridging adjacent particles, contributing to improved interfacial bonding and load transfer capacity within the matrix. The interfacial transition zone between RM particles and the surrounding paste is notably denser compared with the RM10 + FA15 mixture, reflecting a more advanced degree of hydration and pozzolanic reaction at this replacement level. These SEM interpretations, including the densest-microstructure description of RM15 + FA15 noted in the Abstract, are qualitative visual assessments; no image-based quantitative porosity analysis or correlation/regression against the strength and mass-loss data shown in Table 8 was performed, and this microstructure-property relationship should be read as consistent with rather than statistically demonstrated.

At 20% RM replacement, as shown in Figure 14c, the microstructure undergoes notable changes compared with lower replacement levels. While gel formation becomes more abundant due to the increased availability of iron- and alumina-bearing phases from RM, the overall microstructure becomes less homogeneous and more heterogeneous in nature. Partially reacted or unreacted RM particles are more prominently visible, indicating slower dissolution kinetics at higher replacement levels and an insufficient alkaline environment to fully activate the available reactive phases. Spherical FA particles remain clearly identifiable within the matrix at this magnification, suggesting incomplete pozzolanic reaction, likely due to the competitive demand for calcium hydroxide between FA and the increased RM content. Localized porosity zones and microstructural heterogeneity are observed in multiple regions of the matrix, reflecting uneven reaction distribution and incomplete matrix consolidation. Needle-shaped and laminar crystalline phases are also detected at particle boundaries and within the gel matrix, suggesting phase transformation products and potentially the presence of unreacted or partially reacted crystalline compounds from RM. The coexistence of dense gel zones and porous regions within the same microstructure creates weak planes that compromise mechanical integrity and increase susceptibility to sulfate ion ingress. This microstructural heterogeneity is fully consistent with the reduced compressive strength, lower flexural performance, and higher mass loss under sulfate exposure observed for RM20 + FA15 mixtures in the mechanical and durability testing results [49,62,63]. The presence of needle-shaped crystalline phases at higher RM contents also corroborates the observations reported by Pan et al. [8] and Liu et al. [56,59], who attributed similar microstructural features to the formation of iron-rich crystalline reaction products at elevated RM replacement levels. The SEM observations across the three investigated mixtures confirm that increasing RM content from 10% to 20% produces a progressive shift in microstructural characteristics, from a moderately dense matrix with uniform gel distribution at 10% RM, to an optimally compact and homogeneous structure at 15% RM, and finally to a heterogeneous matrix with localized porosity and unreacted residues at 20% RM. The RM15 + FA15 mixture exhibits the most favorable microstructure among the investigated systems, characterized by efficient particle bonding, minimal inter-particle voids, and a well-developed C–S–H gel network, which collectively explain its superior mechanical and durability performance relative to other RM–FA blended mixtures.

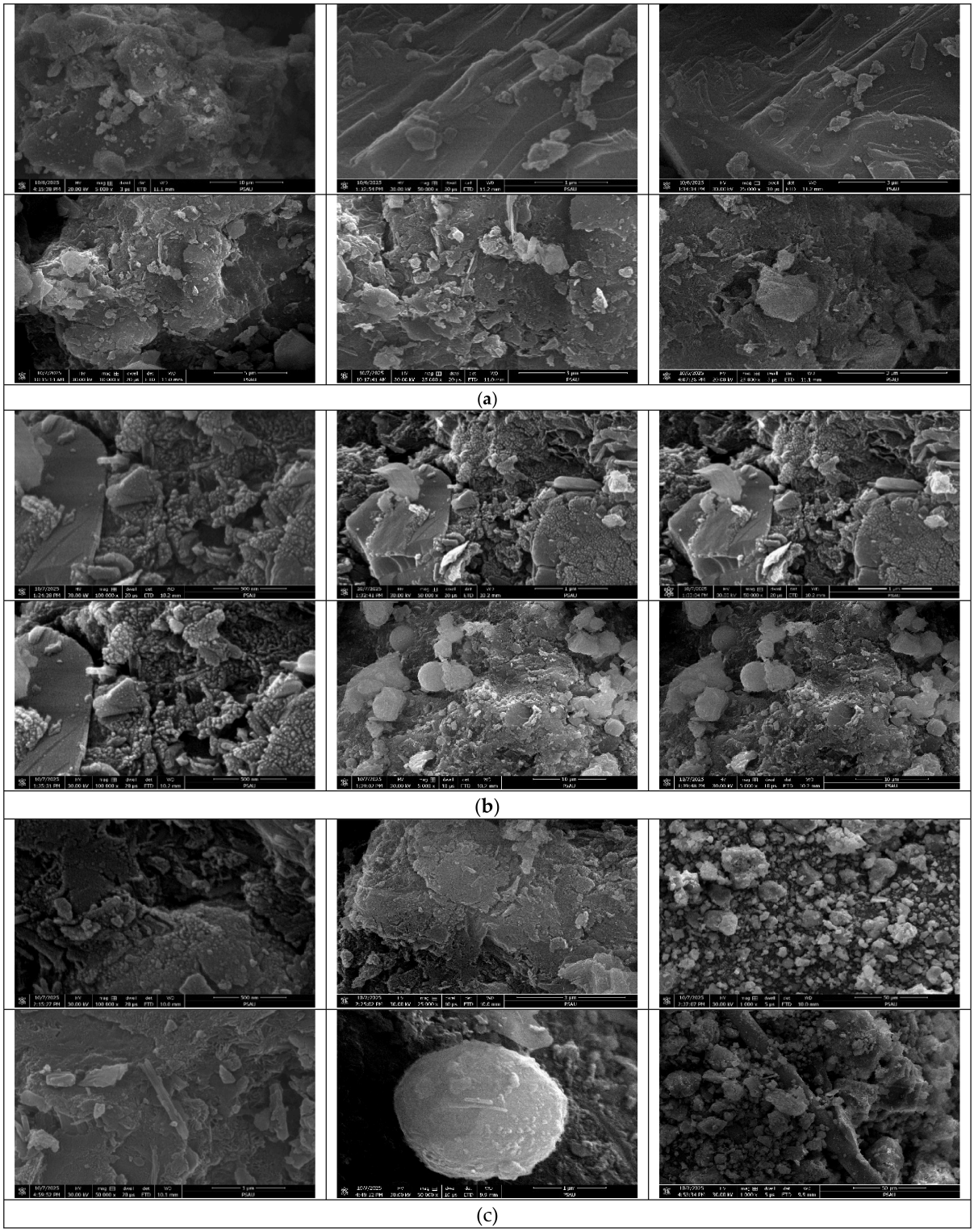


Figure 14. SEM micrographs of cement mortar: (**a**) RM10 + FA15, (**b**) RM15 + FA15, and (**c**) RM20 + FA15.

5. Conclusions

This study investigated the mechanical performance, thermal resistance, durability, and microstructural development of red mud (RM)-based cement mortar incorporating fly ash (FA), basalt fibers (BF), and nano zinc oxide (NZO) as partial cement replacement and reinforcing additions. Based on the experimental findings, the following conclusions can be drawn:

- Red mud (RM) can be effectively valorized as a partial cement replacement through the systematic, individual evaluation of fly ash (FA), basalt fiber (BF), and nano zinc oxide (NZO) within a single RM-based experimental framework, establishing baseline optimal dosages for each constituent as a foundation for future combined-system validation.
- RM incorporation progressively reduced workability and strength through cement dilution and limited hydraulic reactivity, with reductions of up to 35.5% (compressive) and 29.0% (flexural) at 30% RM; 15% FA partially offset these losses via its ball-bearing effect and secondary pozzolanic reactivity, though strength decline resumed beyond 20% RM due to increased matrix heterogeneity.
- BF addition, optimal at 1.5%, provided the most significant single enhancement, increasing compressive and flexural strength by 14.7% and 37.5%, respectively, while also improving residual strength retention at 600–800 °C and reducing sulfate-induced mass loss by 58.9%.
- NZO improved mechanical and durability performance at low dosage (0.5–1.0%), whereas 2.0% NZO represents a critical upper threshold, causing complete mechanical failure and explosive spalling due to agglomeration and C_3S/C_3A hydration retardation.
- SEM analysis confirmed RM15 + FA15 produced the densest, most homogeneous microstructure with minimal voids, corroborating the mechanical and durability trends and supporting a proposed composition of 25% RM, 15% FA, and 1.5% BF.

In summary, RM can be effectively valorized as a partial cement replacement, with FA, BF, and NZO each individually identified as effective performance-enhancing constituents at their respective optimal dosages within the investigated RM-based matrix. Based on the individual optimization of each variable within the experimental matrix, a composition of 25% RM, 15% fly ash, 1.5% basalt fiber, and 0.5% zinc oxide nanoparticles is proposed for future studies; however, this quaternary composition has not been directly tested and requires further experimental validation.

6. Limitations

Despite the valuable findings of this study, several limitations should be acknowledged:

- The mechanical and durability testing was conducted at a single curing age of 28 days. Long-term strength development and durability performance at extended curing ages, such as 90 and 180 days, were not investigated. Furthermore, sulfate resistance was evaluated solely through mass loss, without measuring the compressive strength corrosion coefficient or length change rate, which may be insufficient to capture expansion-type damage mechanisms.
- The study did not address chloride ion penetration resistance or carbonation resistance, which are critical durability indicators for cement-based materials in aggressive environmental conditions.
- Heavy metal leaching behavior (e.g., As, Cr, Pb) from the red mud-based mortar mixtures was not assessed in this study. Compliance with environmental leaching standards must be verified prior to any field application to ensure groundwater safety.
- The elevated temperature testing was limited to 600 °C and 800 °C with a one-hour isothermal exposure period. The behavior of the investigated mixtures under fire scenarios following standardized fire curves, such as ISO 834, was not evaluated. Furthermore, cooling conditions were not systematically documented, and mass change during heating was not recorded, which limits the precision of thermal damage mechanism interpretations.

- The red mud used in this study was sourced from a single alumina refinery. Variability in RM composition from different sources may influence the observed mechanical and durability performance.
- The study did not include advanced mineralogical characterization techniques, such as XRD, FTIR, TG/DSC, or SEM-EDS. Therefore, the proposed hydration products and phase transformation mechanisms were interpreted based on the experimental observations and previous literature rather than being directly confirmed. Future research should incorporate these techniques to verify the proposed reaction mechanisms.

7. Recommendations and Future Work

Based on the findings presented in this research, several recommendations and directions for future research can be proposed to further enhance the understanding and practical applicability of red mud-based mortar systems.

- Long-term mechanical and durability performance of RM-based cement mortar should be investigated at extended curing ages of 90, 180, and 365 days to better understand the contribution of delayed pozzolanic reactions of both RM and FA to strength development.
- The chloride ion penetration resistance, water absorption, and carbonation resistance of the investigated mixtures should be evaluated, in addition to extended sulfate resistance testing incorporating compressive strength, corrosion coefficient, length change rate, and wet–dry cycle accelerated testing, with completely disintegrated specimens discussed separately from comparative mass loss analysis, to provide a more comprehensive assessment of durability performance under aggressive environmental conditions.
- The long-term alkali resistance of basalt fibers in red mud–cement systems should be investigated through alkali-accelerated aging tests at extended curing ages to assess fiber–matrix interfacial durability under the high-pH, sodium-rich environment characteristic of red mud-based mortars.
- Heavy metal leaching tests on optimized red mud-based mortar mixtures should be conducted in accordance with standard leaching methods (e.g., TCLP or EN 12457) to assess the potential release of trace elements such as As, Cr, and Pb, ensuring environmental safety and supporting the sustainability claims associated with red mud valorization in cementitious applications.
- The fire resistance of RM-based mortar systems should be evaluated under standardized fire exposure curves, such as ISO 834, to assess structural performance under realistic fire scenarios and facilitate practical application in fire-resistant construction.
- Comprehensive characterization of the constituent materials, including red mud, fly ash, cement, and nano zinc oxide, should be conducted using particle size distribution (PSD), specific surface area (Blaine/BET), mineralogical analysis (XRD), and nanoparticle dispersion techniques to establish clearer relationships between material characteristics and the fresh, mechanical, and durability performance of red mud-based cement mortars.
- Representative RM-based mortar mixtures should be further characterized using advanced techniques such as XRD, SEM-EDS, FTIR, and TG/DSC to verify the proposed hydration products, phase transformations, nano zinc oxide dispersion, and fiber–matrix interfacial characteristics under different exposure conditions.
- Future studies should investigate the influence of nano zinc oxide dispersion methods, setting behavior, and hydration kinetics through setting time measurements, isothermal calorimetry, and optimized nanoparticle dispersion procedures to better understand the mechanisms governing the performance of high nano zinc oxide dosages in red mud-based cementitious systems.

Author Contributions: Conceptualization, S.A. and A.A.; methodology, M.S.; software, M.S.; validation, M.S. and A.H.A.; formal analysis, M.S.; investigation, A.H.A.; resources, M.S.; data curation, M.S.; writing—original draft preparation, M.S. and A.H.A.; writing—review and editing, A.A.; visualization, A.A.; supervision, S.A.; project administration, M.S.; funding acquisition, S.A. All authors have read and agreed to the published version of the manuscript.

Funding: This research was funded by Prince Sattam bin Abdulaziz University, Ref. PSAU/2025/01/30952.

Institutional Review Board Statement: Not Applicable.

Informed Consent Statement: Not Applicable.

Data Availability Statement: The original contributions presented in this study are included in the article. Further inquiries can be directed to the corresponding author.

Acknowledgments: The authors extend their appreciation to Prince Sattam bin Abdulaziz University for funding this research work through project number (PSAU/2025/01/30952).

Conflicts of Interest: The authors declare no conflicts of interest.

Abbreviations

ANOVA	Analysis of Variance
BF	Basalt Fiber
C–A–S–H	Calcium Aluminosilicate Hydrate
C–S–H	Calcium Silicate Hydrate
CV	Coefficient of Variation
FA	Fly Ash
ITZ	Interfacial Transition Zone
Na_2SO_4	Sodium Sulfate
N–A–S–H	Sodium Aluminosilicate Hydrate
NZO	Nano Zinc Oxide
OPC	Ordinary Portland Cement
RM	Red Mud
SCM	Supplementary Cementitious Material
SD	Standard Deviation
SEM	Scanning Electron Microscopy
SO_4^{2-}	Sulfate Ion
w/b	Water-to-Binder Ratio
XRF	X-ray Fluorescence

References

1. Habert, G.; Miller, S.A.; John, V.M.; Provis, J.L.; Favier, A.; Horvath, A.; Scrivener, K.L. Environmental impacts and decarbonization strategies in the cement and concrete industries. *Nat. Rev. Earth Environ.* **2020**, *1*, 559–573. [CrossRef]
2. Andrew, R.M. Global CO_2 emissions from cement production, 1928–2018. *Earth Syst. Sci. Data* **2019**, *11*, 1675–1710. [CrossRef]
3. Liu, X.; Zhang, N.; Sun, H.; Zhang, J.; Li, L. Structural investigation relating to the cementitious activity of bauxite residue—Red mud. *Cem. Concr. Res.* **2011**, *41*, 847–853. [CrossRef]
4. Power, G.; Gräfe, M.; Klauber, C. Bauxite residue issues: I. Current management, disposal and storage practices. *Hydrometallurgy* **2011**, *108*, 33–45. [CrossRef]
5. Klauber, C.; Gräfe, M.; Power, G. Bauxite residue issues: II. Options for residue utilization. *Hydrometallurgy* **2011**, *108*, 11–32. [CrossRef]
6. Wang, S.; Jin, H.; Deng, Y.; Xiao, Y. Comprehensive utilization status of red mud in China: A critical review. *J. Clean. Prod.* **2021**, *289*, 125136. [CrossRef]
7. Pontikes, Y.; Angelopoulos, G.N. Bauxite residue in cement and cementitious applications: Current status and a possible way forward. *Resour. Conserv. Recycl.* **2013**, *73*, 53–63. [CrossRef]
8. Pan, Z.; Li, D.; Yu, J.; Yang, N. Properties and microstructure of the hardened alkali-activated red mud–slag cementitious material. *Cem. Concr. Res.* **2003**, *33*, 1437–1441. [CrossRef]

9. Ramos, T.; Matos, A.M.; Schmidt, B.; Rio, J.; Sousa-Coutinho, J. Granitic quarry sludge waste in mortar: Effect on strength and durability. *Constr. Build. Mater.* **2013**, *47*, 1001–1009. [CrossRef]
10. Ross, B.E.; Hamilton, H. Evaluation of strain gage lengths for testing limestone and granite aggregate concretes. *Constr. Build. Mater.* **2011**, *25*, 406–408. [CrossRef]
11. Tsakiridis, P.E.; Agatzini-Leonardou, S.; Oustadakis, P. Red mud addition in the raw meal for the production of Portland cement clinker. *J. Hazard. Mater.* **2004**, *116*, 103–110. [CrossRef] [PubMed]
12. Priya, C.B.; Saravanan, T.J.; Balamonica, K.; Gopalakrishnan, N.; Rao, A.R.M. EMI based monitoring of early-age characteristics of concrete and comparison of serial/parallel multi-sensing technique. *Constr. Build. Mater.* **2018**, *191*, 1268–1284. [CrossRef]
13. Ke, X.; Bernal, S.A.; Provis, J.L. Uptake of chloride and carbonate by Mg-Al and Ca-Al layered double hydroxides in simulated pore solutions of alkali-activated slag cement pastes. *Cem. Concr. Res.* **2017**, *100*, 1–13. [CrossRef]
14. Wu, J.; Kim, H. Impacts of road salts on leaching behavior of lead contaminated soil. *J. Hazard. Mater.* **2017**, *324*, 291–297. [CrossRef] [PubMed]
15. Zhang, Z.; Wang, H.; Provis, J.L.; Bullen, F.; Reid, A.; Zhu, Y. Quantitative kinetic and structural analysis of geopolymers. Part 1. The activation of metakaolin with sodium hydroxide. *Thermochim. Acta* **2012**, *539*, 23–33. [CrossRef]
16. Alves, A.R.; Coutinho, A.d.R. The Evolution of the Niobium Production in Brazil. *Mater. Res.* **2015**, *18*, 106–112. [CrossRef]
17. Shu, J.; Kong, D.; Wang, L.; Khan, N.; Zhou, S.; Han, Y.; Tao, T.; Zheng, T. Performance and microstructure of red-mud-blended concrete under different aqueous environments. *Constr. Build. Mater.* **2024**, *447*, 137988. [CrossRef]
18. Lothenbach, B.; Scrivener, K.; Hooton, R.D. Supplementary cementitious materials. *Cem. Concr. Res.* **2011**, *41*, 1244–1256. [CrossRef]
19. Siddique, R. Utilization of coal combustion by-products in sustainable construction materials. *Resour. Conserv. Recycl.* **2010**, *54*, 1060–1066. [CrossRef]
20. Ghalehnovi, M.; Roshan, N.; Hakak, E.; Shamsabadi, E.A.; de Brito, J. Effect of red mud (bauxite residue) as cement replacement on the properties of self-compacting concrete incorporating various fillers. *J. Clean. Prod.* **2019**, *240*, 118213. [CrossRef]
21. Geraldo, V.; de Oliveira, S.; da Silva, E.E.; Oliveira, C.A.d.S.; Cunha, R.M.d.A.; de Oliveira, R.F.P.; Oliveira, C.E.M.; de Morais, E.A. Synthesis of carbon nanotubes on sand grains for mortar reinforcement. *Constr. Build. Mater.* **2020**, *252*, 119044. [CrossRef]
22. Trong, L.N.; Asamoto, S.; Matsui, K. Sorption isotherm and length change behavior of autoclaved aerated concrete. *Cem. Concr. Compos.* **2018**, *94*, 136–144. [CrossRef]
23. Nochaiya, T.; Wongkeo, W.; Chaipanich, A. Utilization of fly ash with silica fume and properties of Portland cement–fly ash–silica fume concrete. *Fuel* **2010**, *89*, 768–774. [CrossRef]
24. Fiore, V.; Scalici, T.; Di Bella, G.; Valenza, A. A review on basalt fibre and its composites. *Compos. Part B Eng.* **2015**, *74*, 74–94. [CrossRef]
25. Sim, J.; Park, C.; Moon, D.Y. Characteristics of basalt fiber as a strengthening material for concrete structures. *Compos. Part B Eng.* **2005**, *36*, 504–512. [CrossRef]
26. Dhand, V.; Mittal, G.; Rhee, K.Y.; Park, S.J.; Hui, D. A short review on basalt fiber reinforced polymer composites. *Compos. Part B Eng.* **2015**, *73*, 166–180. [CrossRef]
27. Al-Rousan, E.T.; Khalid, H.R.; Rahman, M.K. Fresh, mechanical, and durability properties of basalt fiber-reinforced concrete (BFRC): A review. *Dev. Built Environ.* **2023**, *14*, 100155. [CrossRef]
28. Pochwała, S.; Makiola, D.; Anweiler, S.; Böhm, M. The Heat Conductivity Properties of Hemp–Lime Composite Material Used in Single-Family Buildings. *Materials* **2020**, *13*, 1011. [CrossRef] [PubMed]
29. Branston, J.; Das, S.; Kenno, S.Y.; Taylor, C. Mechanical behaviour of basalt fibre reinforced concrete. *Constr. Build. Mater.* **2016**, *124*, 878–886. [CrossRef]
30. Al-Kharabsheh, B.N.; Arbili, M.M.; Majdi, A.; Alogla, S.M.; Hakamy, A.; Ahmad, J.; Deifalla, A.F. Basalt fibers reinforced concrete: Strength and failure modes. *Materials* **2022**, *15*, 7350. [CrossRef] [PubMed]
31. Wang, Y.; Ren, Q.; Xu, J. Influence of basalt fiber on the mechanical properties and deformation failure of concrete after high temperature. *Adv. Civ. Eng.* **2024**, *2024*, 6846792. [CrossRef]
32. Ayub, T.; Shafiq, N.; Nuruddin, M.F. Effect of chopped basalt fibers on the mechanical properties and microstructure of high performance fiber reinforced concrete (HPFRC). *Adv. Mater. Sci. Eng.* **2014**, *2014*, 587686. [CrossRef]
33. Borhan, T.M. Properties of glass concrete reinforced with short basalt fibre. *Mater. Des.* **2012**, *42*, 265–271. [CrossRef]
34. Jiang, C.; Fan, K.; Wu, F.; Chen, D. Experimental study on the mechanical properties and microstructure of chopped basalt fibre reinforced concrete. *Mater. Des.* **2014**, *58*, 187–193. [CrossRef]
35. Nazari, A.; Riahi, S. The effects of ZnO_2 nanoparticles on properties of concrete using ground granulated blast furnace slag as binder. *Mater. Res.* **2011**, *14*, 299–306. [CrossRef]
36. Singh, L.P.; Bhattacharyya, S.K.; Shah, S.P.; Mishra, G.; Ahalawat, S.; Sharma, U. Studies on early stage hydration of tricalcium silicate incorporating silica nanoparticles: Part I. *Constr. Build. Mater.* **2015**, *74*, 278–286. [CrossRef]
37. Li, H.; Xiao, H.G.; Ou, J.P. A study on mechanical and pressure-sensitive properties of cement mortar with nanophase materials. *Cem. Concr. Res.* **2004**, *34*, 435–438. [CrossRef]

38. Liu, J.; Jin, H.; Gu, C.; Yang, Y. Effects of zinc oxide nanoparticles on early-age hydration and the mechanical properties of cement paste. *Constr. Build. Mater.* **2019**, *217*, 352–362. [CrossRef]
39. Khalaf, M.A.; Cheah, C.B.; Ramli, M.; Ahmed, N.M.; Al-Shwaiter, A. Effect of nano zinc oxide and silica on mechanical, fluid transport and radiation attenuation properties of steel furnace slag heavyweight concrete. *Constr. Build. Mater.* **2021**, *274*, 121785. [CrossRef]
40. Nazari, A.; Riahi, S. The effects of ZnO_2 nanoparticles on strength assessments and water permeability of concrete in different curing media. *Mater. Res.* **2011**, *14*, 178–188. [CrossRef]
41. Singh, L.P.; Ali, D.; Tyagi, U.; Sharma, U.; Singh, R.; Hou, P. Durability studies of nano-engineered fly ash concrete. *Constr. Build. Mater.* **2019**, *194*, 205–215. [CrossRef]
42. *ASTM C150/C150M-22*; Standard Specification for Portland Cement. ASTM International: West Conshohocken, PA, USA, 2022. [CrossRef]
43. *ASTM C618-22*; Standard Specification for Coal Fly Ash and Raw or Calcined Natural Pozzolan for Use in Concrete. ASTM International: West Conshohocken, PA, USA, 2022. [CrossRef]
44. *ASTM C311/C311M-22*; Standard Test Methods for Sampling and Testing Fly Ash or Natural Pozzolans for Use in Portland-Cement Concrete. ASTM International: West Conshohocken, PA, USA, 2022.
45. *ASTM E1621-22*; Standard Guide for Elemental Analysis by Wavelength Dispersive X-Ray Fluorescence Spectrometry. ASTM International: West Conshohocken, PA, USA, 2022.
46. *ASTM C1437-20*; Standard Test Method for Flow of Hydraulic Cement Mortar. ASTM International: West Conshohocken, PA, USA, 2020. [CrossRef]
47. *ASTM C109/C109M-21*; Standard Test Method for Compressive Strength of Hydraulic Cement Mortars (Using 2-in. or [50-mm] Cube Specimens). ASTM International: West Conshohocken, PA, USA, 2021. [CrossRef]
48. *ASTM C348-21*; Standard Test Method for Flexural Strength of Hydraulic-Cement Mortars. ASTM International: West Conshohocken, PA, USA, 2021. [CrossRef]
49. *ISO 834-1:1999*; Fire-Resistance Tests, Elements of Building Construction, Part 1: General Requirements. International Organization for Standardization: Geneva, Switzerland, 1999.
50. Ma, J.; Wang, D.; Zhao, S.; Duan, P.; Yang, S. Influence of Particle Morphology of Ground Fly Ash on the Fluidity and Strength of Cement Paste. *Materials* **2021**, *14*, 283. [CrossRef] [PubMed]
51. Tole, I.; Delogu, F.; Qoku, E.; Habermehl-Cwirzen, K.; Cwirzen, A. Enhancement of the pozzolanic activity of natural clays by mechanochemical activation. *Constr. Build. Mater.* **2022**, *352*, 128739. [CrossRef]
52. Li, Z.; Wang, H.; He, S.; Lu, Y.; Wang, M. Investigations on the preparation and mechanical properties of the nano-alumina reinforced cement composite. *Mater. Lett.* **2006**, *60*, 356–359. [CrossRef]
53. Liu, M.; Guo, Z.; Qian, Y.; Chen, L.; Mao, X.; Zhao, J.; Yang, D. Investigation into the long-term alkali resistance of basalt fibers. *J. Build. Eng.* **2024**, *98*, 111105. [CrossRef]
54. Fujii-Yamagata, A.; Cardoso, F.; Sarou-Kanian, V.; Daubresse, A.; Prat, E.; Chaouche, M. Skin formation in adhesive mortars evaluated by MRI and interfacial rheology. *Cem. Concr. Compos.* **2019**, *99*, 251–261. [CrossRef]
55. Li, S.; Chen, G. Agricultural waste-derived superabsorbent hydrogels: Preparation, performance, and socioeconomic impacts. *J. Clean. Prod.* **2020**, *251*, 119669. [CrossRef]
56. Liu, Z.-H.; Ding, Y.-D.; Wang, F.; Deng, Z.-P. Thermal insulation material based on SiO_2 aerogel. *Constr. Build. Mater.* **2016**, *122*, 548–555. [CrossRef]
57. Zhang, Z.; Zhang, D.; Zhou, J.; Zhang, D.; Tan, K.H. A critical review on high temperature performance of sustainable cementitious materials. *npj Mater. Sustain.* **2025**, *3*, 39. [CrossRef]
58. da Silva, G.; Martini, S.; Moraes, J.; Teles, L. AC impedance spectroscopy (AC-IS) analysis to characterize the effect of nanomaterials in cement-based mortars. *Constr. Build. Mater.* **2021**, *269*, 121260. [CrossRef]
59. Liu, C.; Chen, J. High temperature degradation mechanism of concrete with plastering layer. *Materials* **2022**, *15*, 398. [CrossRef] [PubMed]
60. Amiri, M.; Aryanpour, M.; Porhonar, F. Microstructural study of concrete performance after exposure to elevated temperatures via considering C–S–H nanostructure changes. *High Temp. Mater. Process.* **2022**, *41*, 224–237. [CrossRef]
61. Land, G.; Stephan, D. The effect of synthesis conditions on the efficiency of C-S-H seeds to accelerate cement hydration. *Cem. Concr. Compos.* **2018**, *87*, 73–78. [CrossRef]
62. Lobo-Sánchez, M.; Nájera-Meléndez, G.; Luna, G.; Segura-Pérez, V.; Rivera, J.A.; Fetter, G. ZnAl layered double hydroxides impregnated with eucalyptus oil as efficient hybrid materials against multi-resistant bacteria. *Appl. Clay Sci.* **2018**, *153*, 61–69. [CrossRef]
63. Zhai, S.; Song, K.; Ding, C.; Wang, Y.; Dong, Y.; Zhao, X. Tunable Acoustic Metasurface with High-Q Spectrum Splitting. *Materials* **2018**, *11*, 1976. [CrossRef] [PubMed]
64. Sutar, H.; Mishra, S.C.; Sahoo, S.K.; Chakraverty, A.P.; Maharana, H.S. Progress of red mud utilization: An overview. *Am. Chem. Sci. J.* **2014**, *4*, 255–279. [CrossRef]

65. Duan, H.; Xie, Y.; Zou, L.; Li, B.; Håkansson, U.; Cvetkovic, V. Analysis of grout radial propagation in water-saturated rough-walled rock fractures. *Int. J. Rock Mech. Min. Sci.* **2025**, *190*, 106101. [CrossRef]
66. Duan, H.; Zou, L.; Li, B.; Håkansson, U.; Cvetkovic, V. Effect of rheological model selection on prediction of cement grout propagation in rock fractures. *Int. J. Rock Mech. Min. Sci.* **2026**, *202*, 106523. [CrossRef]
67. Hao, M.; Song, S.; Duan, H.; Li, X.; Zhong, Y.; Zhang, J. Effect of fracture aperture on propagation properties of self-expanding polyurethane grout. *Constr. Build. Mater.* **2025**, *458*, 139496. [CrossRef]

Disclaimer/Publisher's Note: The statements, opinions and data contained in all publications are solely those of the individual author(s) and contributor(s) and not of MDPI and/or the editor(s). MDPI and/or the editor(s) disclaim responsibility for any injury to people or property resulting from any ideas, methods, instructions or products referred to in the content.